Deglaciation and abrupt events in a coupled comprehensive atmosphere–ocean–ice sheet–solid earth model

Uwe Mikolajewicz[1], Marie-Luise Kapsch[1], Clemens Schannwell[1], Katharina D. Six[1], Florian A. Ziemen[1,2], Meike Bagge[3,4], Jean-Philippe Baudouin[5], Olga Erokhina[1,6], Veronika Gayler[1], Volker Klemann[3], Virna L. Meccia[1,7], Anne Mouchet[1,8], and Thomas Riddick[1]

[1]Max Planck Institute for Meteorology, Hamburg, Germany
[2]now at: Deutsches Klimarechenzentrum, Hamburg, Germany
[3]Helmholtz Centre Potsdam, German Research Centre for Geosciences - GFZ, Potsdam, Germany
[4]now at: Federal Institute for Geosciences and Natural Resources, Hannover, Germany
[5]Department of Geosciences, University of Tübingen, Tübingen, Germany
[6]now at: Astronomisches Rechen-Institut, Center for Astronomy of Heidelberg University, Heidelberg, Germany
[7]now at: National Research Council, Institute of Atmospheric Sciences and Climate, Bologna, Italy
[8]now at: GeoHydrodynamics and Environment Research, University of Liège, Liège, Belgium

Correspondence: Uwe Mikolajewicz (uwe.mikolajewicz@mpimet.mpg.de)

Abstract.

During the last 20,000 years the climate of the earth has changed from a state much colder than today with large ice sheets in North America and Northwest Eurasia to its present state. The fully-interactive simulation of this transition represents a hitherto unsolved challenge for state-of-the-art climate models. We use a novel coupled comprehensive atmosphere–ocean–vegetation–ice sheet–solid earth model to simulate the transient climate evolution from the last glacial maximum to preindustrial times. The model considers dynamical changes of the glacier mask, land–sea mask and river routing. An ensemble of transient model simulations successfully captures the main features of the last deglaciation, as depicted by proxy estimates. In addition, our model simulates a series of abrupt climate changes, which can be attributed to different drivers. Sudden weakenings of the Atlantic meridional overturning circulation during the glacial and the first half of the deglaciation are caused by Heinrich-event like ice-sheet surges, which are part of the model generated internal variability. We show that the timing of these surges depends on the initial state and the model parameters. Abrupt events during the second half of the deglaciation are caused by a long-term shift in the sign of the Arctic freshwater budget, changes in river routing and/or the opening of ocean passages.

1 Introduction

The last deglaciation is marked as the transition from the cold climate of the Last Glacial Maximum (LGM; about 21 kiloyears before present, hereafter referred to as ka) to the modern climate. Driven by gradual changes of the orbital parameters and increasing atmospheric CO_2 concentrations, the climate warmed by several Kelvin and the massive ice sheets over North America and North Eurasia vanished, leading to a strong rise in sea level. Reconstructions of the global mean sea level show a monotonic rise, although with strong temporal variations in the rates of sea level change (e.g., **??**). During the main phase

of the deglaciation, from 16.5 to 8 ka, the average rate of 12 m ka^{-1}, corresponding to approx. 0.14 Sv (1 Sv = 10^6 m^{3}s^{-1})

net meltwater input (**??**), varied between periods with greater values, e.g. during the meltwater pulse 1A (MWP1A, about 14.7 to 13.5 ka; e.g. **????**) with meltwater input rates close to 0.5 Sv (**??**), and smaller values, e.g. during the Younger Dryas (YD, about 12.8 to 11.7 ka, e.g., **?**). During the glacial and the early deglaciation, several abrupt cooling events can be detected in sediment cores from the North Atlantic containing prominent layers of ice-rafted debris, which originate from melted icebergs that were released from the Laurentide ice sheet into the North Atlantic (**?**). Any addition of large amounts of freshwater into the North Atlantic, whether through melting of icebergs or the direct release of meltwater from the ice sheets themselves, affects the surface salinity, reduces the deepwater formation and weakens the Atlantic meridional overturning circulation (AMOC). As a result, the northward heat transport reduces and lowers the release of ocean heat into the atmosphere, causing large-scale climate changes. Examples of abrupt events are the cold Heinrich Stadial 1 (H1; about 16.8 ka; **?**), the YD, or the rapid Bølling-Allerød (BA) warming, which occurred in between H1 and the YD (about 14.7 to 14.2 ka; e.g. **????**).

Various proxy data from marine sediment cores have been used to assess the AMOC state for the glacial climate (**?**) and its variability (**???**). These data indicate the existence of abrupt climate events, which shaped the sediment record, but even a qualitative estimate of changes in the characteristics of the AMOC remains challenging. For example, even the sign of the AMOC variations is still unclear(e.g. **?**). The common consensus, based on studies of the stable δ^{13}C isotope or neodymium, is that the position of the AMOC core was shallower during the LGM compared to modern day, but from the current set of available proxy data, it is unclear if and how much the AMOC strength may have changed in comparison to modern state (see e.g. review of **?**). From an ensemble of simulations with an Earth System Model of Intermediate Complexity (EMIC) with different AMOC strengths and four proxy tracers, **?** concluded that the global proxy distributions can only be reconciled with an ocean state characterized by a relatively weak AMOC showing a reduction in the circulation strength by $36 \pm 8\%$ (6.3 $\pm$ 1.4 Sv) relative to that of the pre-industrial state (PI). However, the sources of uncertainty in this methodology are numerous and diverse. They include an incomplete understanding of the recording and storing of climate signals through proxy data (**??**), as well as a methodological weakness in the reconstruction of the water mass mixing based on proxy data (e.g. **????**).

Despite the evidence of abrupt events during the deglaciation from proxies, the causes of the abrupt warming and cooling events and their link to AMOC variations remain uncertain. To understand the AMOC variability and its drivers, therefore requires modelling approaches that span the entire deglaciation. Early modelling studies focused on exploring hypotheses around abrupt events with idealised sensitivity experiments, such as the effect of meltwater release from the ice sheets on the stability of the AMOC (**????**). More recently, the performance of comprehensive coupled climate/earth system models containing both atmospheric and oceanic general circulation model components, as have been used in the Coupled Model Intercomparison Project (CMIP), and their sensitivities to climate perturbations have been evaluated in time slice experiments of, for example, the LGM or PI (e.g. **??**). Historically, these models have been developed for the simulation of time periods in which changes in the topography and the ice sheets can be neglected. This assumption, does not hold for the last deglaciation and, together with computational demands, represents one of the technical challenges that in large parts explains the paucity of transient simulations covering the last deglaciation with comprehensive climate models. Furthermore, transient deglaciation simulations have so far relied on prescribed ice sheets from reconstructions (**??????**). Several studies have highlighted that the transient

climate response in such simulations, particularly around abrupt events, is dominated by the choice of ice sheet reconstruction
and their type of meltwater forcing (**???**). A primary example is the meltwater release associated with MWP1A. The main ice
sheet reconstructions utilised in PMIP4 (**???**) suggest strong meltwater forcing in excess of 0.4 Sv in the northern hemisphere
for MWP1A. The meltwater release of MWP1A into the North Atlantic results in an AMOC weakening, and cold surface
temperatures in the northern hemisphere. This is not consistent with the subsequent BA warm period as recorded in the Green-
land temperature records (**?**). This discrepancy between the prescribed meltwater forcing from ice-sheet reconstruction and the
ensuing climate response advocates for the inclusion of interactive ice sheets into climate models. However, because of the
long characteristic time scales involved in the modelling of ice sheets, they have been mainly included in EMICS (**????**). The
reduced physics, which EMICs are based on, permit the longer integration times necessary for these simulations. Coupling
of interactive ice sheets into more computationally expensive comprehensive climate models has so far focused mainly on
shorter time scales up to two millennia (e.g. **???????**). However, previous modelling efforts often included only a subset of the
ice sheets (**???**). In addition, these type of studies typically employed coupling routines, in which the more computationally
expensive climate model was accelerated (**???**), and did not explicitly account for iceberg or solid earth interactions.

Here we present results from a novel model system that consists of a coarse resolution version of a comprehensive climate
model, includes interactive ice sheets for both hemispheres as well as iceberg and solid earth interactions, and is applied to
the last deglaciation. The model system is described in section 2 and its performance is evaluated for the LGM and PI time
slices (Section 3.1). We then present an ensemble of transient simulations of the last deglaciation with the new model system
(Section 3.2) before we focus on the consequences and control of abrupt AMOC-related climate events that are triggered by
ice-sheet and topography changes and the associated climate response (Sections 4.1 and 4.2). The main findings are sum-
marised in section 5.

2   Model and experiment description

2.1   Model

The model system MPI-ESM/mPISM/VILMA consists of a coupled atmosphere–ocean-vegetation–ice sheet–solid earth model.
A schematic of the coupled model system is shown in Fig. 1. We provide here only a very brief description of the individual
components to focus on the scientific applications.

The climate model is the coarse resolution version of Max Planck Institute for Meteorology Earth System Model (MPI-ESM)
version 1.2 (**??**) that also has been used for the deglacial simulation described in **?**. The atmospheric component is ECHAM6.3
(**?**). It has a spectral resolution of T31 (corresponding to approx. 3.75° on a Gaussian grid) and 31 levels in the vertical on
hybrid coordinates. Land surface processes and vegetation dynamics on land are treated by the JSBACH component (**?**). A
hydrological discharge model (**?**) transports the runoff from land to the ocean.
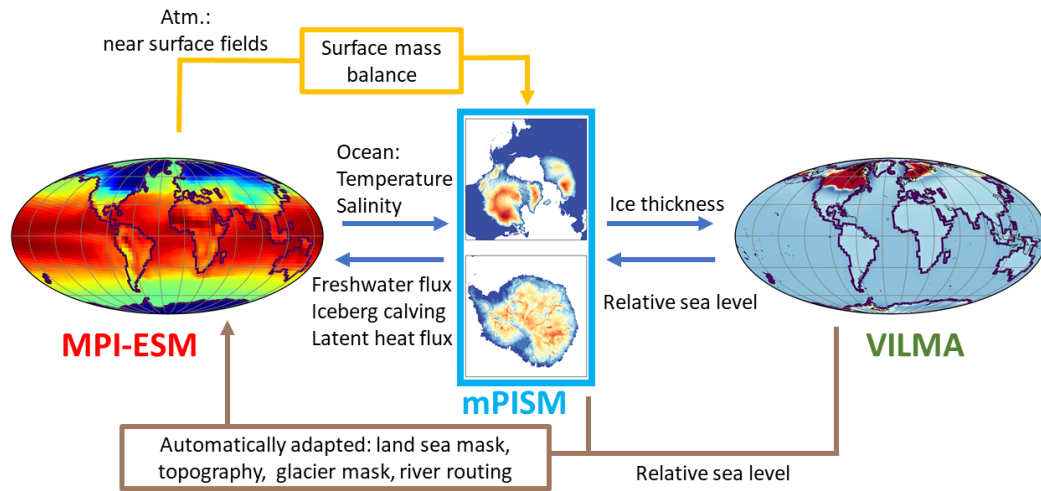
Figure 1. Schematic of the model framework MPI-ESM/mPISM/VILMA with its individual components MPI-ESM, mPISM, and VILMA and the information exchange between the components. As an example, one characteristic property is shown for each model component: surface temperature for MPI-ESM, ice-sheet thickness for mPISM, and relative sea level change for VILMA.

The ocean component is MPIOM1.6 (**?**). It has a resolution of 3° on an Arakawa C grid (**?**) with the grid poles located in southeast Greenland and in the centre of Antarctica, yielding a relative high resolution in the North Atlantic subpolar gyre (35 to 150 km). The ocean model has 40 levels on z-coordinates, with layer thickness increasing towards depth, a free surface and a mass flux boundary condition. Vertical mixing and diffusion are based on a Richardson-number dependent formulation by **?**. In addition, a simple mixed-layer scheme describes near-surface mixing. For the background mixing, a fixed vertical profile is assumed. Starting with a given surface value, it increases linearly with depth until 1000 m. Below it is constant. A sea-ice component with viscous plastic rheology following **?** with 0-layer thermodynamics including snow is embedded in MPIOM. In addition, the version of MPIOM used here contains a new dynamic/thermodynamic Eulerian iceberg model with 5 size classes (**?**), allowing the explicit treatment of calved icebergs, their subsequent drift and a 3-dimensional input of meltwater and latent heat release.

For the assessment of the past circulation changes, proxy data are the only source of information. Therefore, we included an artificial water mass tracer (dye) in the ocean component to gain a better insight into how circulation changes would be reflected in proxy data. The dye indicates the relative contribution of water originating from the surface of the North Atlantic and the Arctic, and thus is tracing the relative contribution of North Atlantic Deep Water (NADW) at depth. The boundary condition of the dye at the surface is 1 in the source area (see Fig. A2) and 0 outside this area. In the ocean interior, the dye is advected and mixed like salinity.

Ice sheets are represented by the thermomechanically-coupled ice-sheet model mPISM (**?**) based on PISM0.7.3. The ice dynamics in mPISM are based on the superposition of the shallow-ice and shallow-shelf approximations, making it suitable to model slow ice flow, fast ice flow as well as grounding-line migration. The polar stereographic grid has a resolution of 10 km in the northern hemisphere and 15 km for Antarctica. The surface mass balance (SMB) of the ice sheet is calculated by an energy balance model using hourly atmospheric input data from the atmospheric model component ECHAM6.3 (**?**) on 24 different height levels on the atmospheric grid. This 3-dimensional SMB field is then interpolated onto the actual surface topography of the ice sheet model.

The response of the solid Earth and changes in relative sea level, induced by the consistent redistribution of ice and water masses are computed with the global VIscoelastic Lithosphere and MAntle model (VILMA, **?**). VILMA is employed in its 1D configuration, which assumes that the viscosity structure of the Earth varies only with depth. VILMA solves the sea-level equation, accounts for rotational feedback and considers an incompressible self-gravitating viscoelastic material with a Maxwell rheology. The sea level equation is solved on the horizontally discretized Gaussian F128 grid (approx. $0.7°$), which represents the resolution at which data are exchanged, i.e. the ice sheet distribution as input and the negative relative sea level change, representing the change in topography due to glacial isostatic adjustment (e.g., **?**).

The coupling time step between the atmosphere and ocean model is one day. The iceberg model is part of the ocean model and thus interacts on every ocean time step. The ESM is coupled every 10 years with the ice sheet and solid earth models. At this interval, new high resolution topographies ($1/6°$ horizontal resolution) are calculated from the results of VILMA and mPISM and used to derive adapted topographies (incl. land/sea masks) for the ocean and the atmosphere using the algorithm developed by **?**. River routing directions are adapted dynamically according to topography changes using the algorithm developed by **?**. The ice sheet model supplies calving fluxes to the iceberg module. A reduced version of this model system without icebergs, ice sheet and solid Earth dynamics has been used by **?** to perform deglacial simulations using prescribed ice sheet reconstructions.

2.2 Experiments

For all simulations, the atmospheric concentrations of CO_2, CH_4 and N_2O were prescribed according to **?**. Earth orbital parameters were calculated following **?**. In addition, in most simulations, annually varying volcanic forcing (**?**) was prescribed for the time after 26 ka.

To achieve a physically-consistent initial state for 26 ka, transient asynchronous spin-up simulations were started from one existing glacial state of the model system. These asynchronous simulations cover the period from 45 to 26 ka. During the asynchronous spin-up, MPI-ESM was run for 10 years providing the forcing for a 100 year simulation with mPISM and VILMA. Subsequently, freshwater/iceberg supply from the ice sheets and topography/bathymetry changes from mPISM/VLIMA are considered in the next 10 year simulation with MPI-ESM. This procedure was repeated over the entire asynchronous spin-up period from 45 to 26k̃a, yielding a spin-up of 19,000 years for mPISM/VILMA and 1,900 years for MPI-ESM. This accelera-

135 tion of a factor 10 saves considerable amounts of computing time and serves to spin-up the model components with the longest memory. A climatological volcanic forcing was used in the spin-up integrations to avoid large artificial variability.

A set of eight synchronously coupled transient deglacial experiments with different model parameter settings were started from asynchronous spin-up simulations at 26 ka. For an overview of the ensemble members see Table 1.

We do not consider the first 1000 years for our analysis to circumvent the effects of minor adjustments after the switch to the

140 synchronously coupled simulation. Thus, our analysis covers only the time from 25 ka to 1850 CE. For the LGM time slice, the simulations had a spin-up for atmosphere and ocean without parameter changes for 4,900 years (3,000 years for D1.2 and D1.3) ensuring sufficient adjustment time to the transient forcing.

Effectively, our full ensemble consists of two smaller, separate sub-ensembles, each containing four members. The first sub-ensemble explores the effect of vertical mixing in the ocean. **?** used a combination of a tidal model and an EMIC to investigate

145 the effect of enhanced tides during the glacial and reports a change of global mean diapycnal mixing of more than a factor of 3 compared to PI. Since the background mixing is rather poorly constrained and includes in our mixing scheme a variety of processes, e.g. tidal mixing, we investigated the sensitivity to this parameter in the first sub-ensemble. Here, D1.1 serves as the baseline experiment. All four members of this sub-ensemble start from the same asynchronous spin-up simulation. In experiment D1.2 the vertical background mixing coefficient was increased while in experiment D1.3 it was decreased. All

150 experiments of this sub-ensemble used a climatological volcanic forcing representing PI with the exception of D1.4, which was forced with the time-varying volcanic forcing (**?**).

For the second sub-ensemble, D2.1 is the baseline experiment. In comparison to D1.1, several parameter values within the individual ESM components were changed. This includes changes in sea-ice parameters towards a more rigid sea ice (like e.g. **?** in comparison to **?**) and reduced drag between the ocean and sea ice. The latter is motivated by the fact that the katabatic

155 winds and consequently the sea ice transports in this model are somewhat underestimated due to the coarse resolution of the atmospheric component. Additionally, the prescribed vertical profile of oceanic background mixing was reduced in the upper ocean. This was motivated by the results of the first ensemble, which show a large effect of the prescribed background mixing on the AMOC (see section 3.1), but also a strong effect on the age distribution of the water masses especially in the Pacific (not shown). To maintain both a reasonable age distribution in the deep ocean for PI as well as a more realistic glacial AMOC,

160 the reduced mixing was restricted to the upper ocean. As the treatment of the ocean surface velocities in the coupling interface of the atmosphere was discovered to be affected by a bug, this part of the coupling was suppressed in all simulations of this sub-ensemble. To maintain a similar climate in terms of the surface temperatures, small changes in the atmospheric parameters were required to reduce a slight cold bias. Changes in the ice-sheet parameters in comparison to the first sub-ensemble focused on enhanced sliding and a more sensitive basal mass balance. The goal behind the enhanced sliding tuning was two-fold:

165 first, we targeted a faster expansion of the ice sheets towards the LGM; second, the resulting thinner ice sheets facilitate ice sheet retreat during the deglaciation. The more sensitive basal mass balance was targeted towards a faster retreat of the marine portions of the Antarctic ice sheets. All runs in this sub-ensemble were run with time-varying volcanic forcing and start from their own matching asynchronous spin-up.
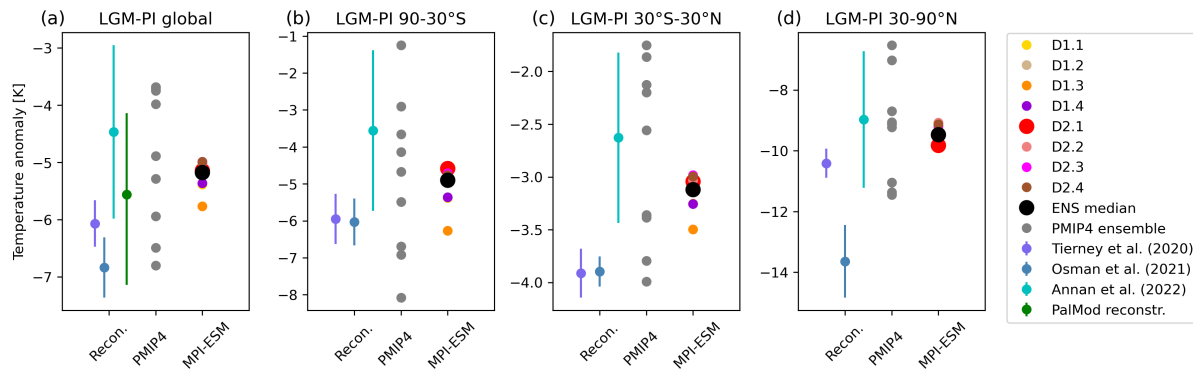
Figure 2. Mean annual surface air-temperature anomalies in K with respect to PI for different regions: (**a**) the global mean, the mean over (**b**) the southern extratropics (90°-30° S), (**c**) the tropics (30° S-30° N) and (**d**) the northern extratropics (30°-90° N). Each panel shows values derived from reconstructions (left) (**?????**, and the PalMod reconstructions), the PMIP4 model ensemble (center **?**) and our model ensemble (right). Whiskers on the reconstructions indicate uncertainties.

In addition, two sensitivity experiments (D2.1.1 and D2.1.2) were performed to investigate the effect of initial conditions for the ice sheets on the deglacial climate trajectory. Except for the initial conditions they are identical to D2.1. These experiments are analyzed in Section 4.2 and are not included in our main ensemble. Experiment D2.1.1 was only integrated until 7 ka.

3 The simulated climate

To evaluate the simulated climate, we first show the model results for the time of the LGM. The LGM has been intensively investigated for steady state time-slice simulations (21 ka), as it is a standard time slice within the Paleo Modeling Intercomparison Project Phase 4 (PMIP4) (e.g. **?**). In subsection 3.2 we will present the simulated transient deglacial climate changes.

3.1 LGM climate relative to PI

Since our model runs show substantial millennial-scale variability throughout the glacial (see Section 4.2), we chose to average the LGM state over the time window from 23 ka to 18 ka. In the Holocene, millennial scale variability is rather small, thus only 1000 years (1100 to 100 yrBP) were used for the calculation of the PI climate state. In addition to the ensemble median, minimum and maximum, we also show results from one particular experiment (D2.1), which we use in Section 4.1 to discuss the deglacial climate variability in more detail.

Near-surface air temperatures

The simulated global mean LGM near-surface air temperature (SAT) in our model ensemble is 5.0 to 5.8 K colder than the PI reference state (Fig. 2 a). The simulated cooling pattern shows a strong polar amplification illustrated by the significantly

Table 1. Ensemble members with their parameter settings and spin-up procedures. Detailed individual parameter changes are listed in Table A1 and A2. In all asynchronous spin-up simulations climatological volcanic forcing was used.

Name	MPI-ESM	Volcanoes	PISM_ANT	PISM_NH	Asynchronous spin-up
D1.1	version 1	fixed	version 1	version 1	- parameters as in synchronous simulation
D1.2	version 1 - increased background diffusivity in the ocean	fixed	version 1	version 1	- parameters as in synchronous simulation D1.1
D1.3	version 1 - decreased background diffusivity in the ocean	fixed	version 1	version 1	- parameters as in synchronous simulation D1.1
D1.4	version 1	varying	version 1	version 1	- parameters as in synchronous simulation D1.1
D2.1	version 2 - reduced background mixing in the upper ocean - more rigid sea ice - atmosphere retuned	varying	version 2 - enhanced sliding near grounding line - increased basal melt	version 2 - enhanced sliding - increased basal melt	- parameters as in synchronous simulation
D2.2	version 2 - atmosphere as in version 1	varying	version 2	version 2	- parameters as in synchronous simulation
D2.3	version 2 - brighter albedos in smb-EBM	varying	version 2	version 2	- parameters as in synchronous simulation
D2.4	version 2	varying	version 1 - decreased sliding near grounding line	version 2	- parameters as in synchronous simulation
D2.1.1 [a,b]	version 2	varying	version 2	version 2	- parameters as in synchronous simulation D2.1 - ice sheets from 27 ka
D2.1.2 [a]	version 2	varying	version 2	version 2	- parameters as in synchronous simulation D2.1 - ice sheets from 28 ka

[a] The sensitivity studies D2.1.1 and D2.1.2 are not part of the ensemble, [b] D.2.1.1 was run only until 7 ka

185 larger cooling in the high northern latitudes (9.1 to 9.8 K) than in the tropics (between 3.0 and 3.5 K; Fig. 2d and c). In the southern high latitudes, the simulated LGM climate is between 4.6 and 6.3 K (mean: 5.1; median: 4.8) colder (Fig. 2b). These

values lie well within the LGM (21 ka) climate signal from the PMIP4 ensembles (3.7 to 6.8 K). Our estimates also agree well with estimates of LGM near-surface air temperature anomalies from available reanalysis/reconstruction data sets (see Fig. 2). For validation, we use recent products either based entirely on proxy data (such as the PalMod reconstructions, based on the methodology and proxy data described in **?**, see Appendix A2) or data assimilation products that use either a single model (**??**) or an ensemble of models (**?**). Globally, our simulated SAT anomalies (mean: -5.2 K; median: -5.1 K) align with the range of reconstructed SAT anomalies of the PalMod reconstructions (Appendix A2) of -4.1 and -7.1 K (mean: -5.6 K) and the reanalysis of **?** of -6.5 to -3.5 K (mean: -5.0 K) and **?** of -2.9 to -6.0 K (mean: 4.5 K). The reanalyses of **?** and **?** and to a smaller extent the reconstructions of **?** are consistently colder than our ensemble (-6.3 to -7.4 K, -5.7 to -6.5 K, and -7.5 to -5.1 K, respectively) and the **?** data assimilation product. The same signal is present through regional estimates for the northern and southern extratropics and tropics, where our ensemble mean is slightly colder than **?** but warmer than **?** and **?**. Thereby nearly all ensemble members fall into the uncertainty range of the **?** estimates, except for D1.3 for the tropics and southern extratropics.

Maximum cooling is simulated over the Laurentide and Fennoscandian ice sheets (Fig. 3), where the higher surface elevation leads to an additional cooling effect. Also the North Atlantic shows a rather strong cooling, which is related to extended sea-ice cover (Fig. 3). In general, the simulated pattern of cooling is rather similar to the ensemble mean pattern from the CMIP6 LGM time-slice simulations (**?**, their Fig. 1) and the reanalysis product of **?**. The spatial pattern of the reanalysis product by **?** is also very similar to our ensemble, but the amplitude of the cooling is considerably stronger. The bias of the simulated PI near surface air temperature and sea ice edge compared to an observation based estimate is shown in Fig. A1.

Sea-ice extent

The simulated sea-ice extent on the northern hemisphere for the PI period is fairly close to the extent derived from the HadiSST data set for the years 1951 to 1990 (**?**) (see isolines in Figs. 3 and A1). The main discrepancy is an underestimation of the sea-ice extent in the Southern Ocean.

For the LGM, the ensemble spread for the winter sea-ice extent in the North Atlantic is considerable. Some simulations show an ice-free Northeast Atlantic, others a state with winter sea ice that covers nearly the entire North Atlantic north of 40° N. The Northwest Atlantic is seasonally sea ice covered in all simulations. In the North Atlantic, the GLOMAP reconstruction (**?**) does not show a large difference between the Northwest and Northeast Atlantic. It is worth noting that the simulation D2.1 does not show such a contrast either. The Norwegian Sea is only seasonally covered by sea ice in all simulations, whereas most of the Greenland and Icelandic Sea are permanently covered by sea ice. GLOMAP indicates seasonal sea-ice cover in the entire Nordic Seas, with the LGM summer sea-ice margin even being north of its position in the 20th century in the HadiSST data set (**?**). The simulated Southern Ocean sea-ice cover is seasonal, except for some regions close to the coast of Antarctica. The model generally underestimates the summer sea-ice extent in the southern hemisphere, both for PI as well as for LGM. The simulated winter sea-ice extent in the Southern Ocean matches the GLOMAP data set well.
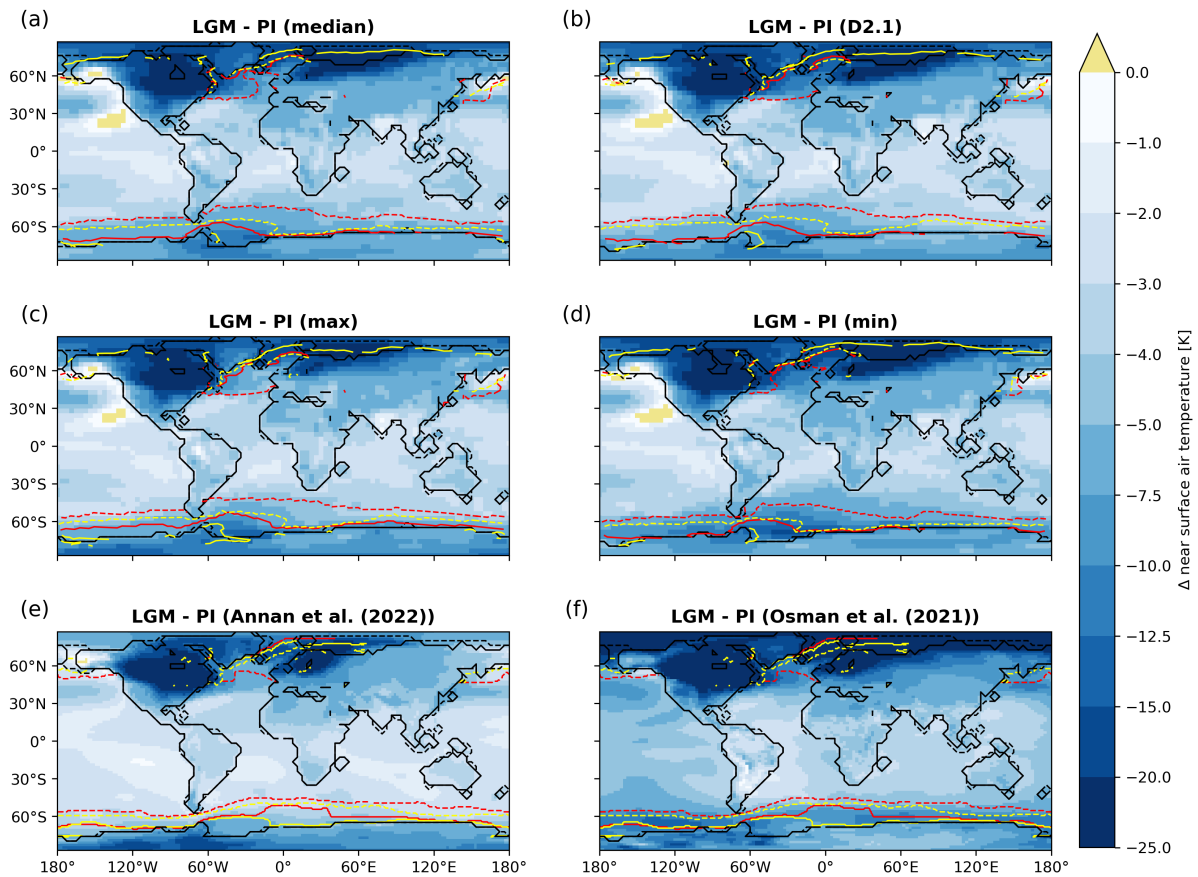
Figure 3. Difference in annual mean near-surface air temperature between LGM and PI in K (colours). The panels show (a) the ensemble median, (b) the results for simulation D2.1, (c) the ensemble maximum, and (d) the ensemble minimum. Please note ensemble minimum/-maximum indicates the minimum/maximum value occurring in any of the ensemble members at each grid point. The isolines show sea-ice extent (> 0.15 sea-ice coverage in the long-term mean seasonal climatology) for PI summer (yellow solid) and winter (yellow dashed) and LGM summer (red solid) and winter (red dashed). The bottom panel shows reanalysis results from (e) **?** and (f) **?**. The LGM sea-ice margin plotted in the bottom panels is taken from the GLOMAP (**?**) reconstruction, the PI reference has been calculated from years 1951 to 1990 from the HadiSST data set (**?**). PI and LGM land–sea masks are indicated by the solid and dashed black lines, respectively.
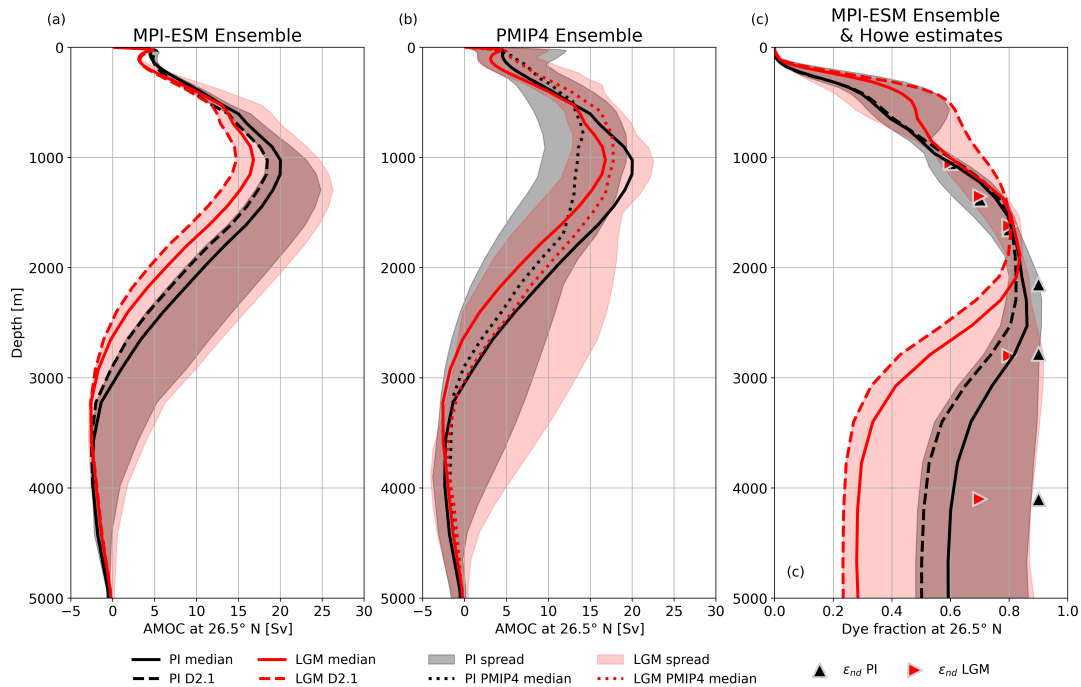
Figure 4. (a) Depth profiles of the simulated AMOC at 26.5° N for the ensemble median (solid lines) and the ensemble spread (shadings) for PI (black) and LGM (red). Dashed lines highlight the results of D2.1. (b) Same as (a), but based on the PMIP4 ensemble (**?**) with the ensemble median given as dotted line. For better comparison, the ensemble medians from (a) is shown as well (solid lines). (c) Depth profiles of the zonally averaged relative contribution of water originating from the surface of the North Atlantic or the Arctic at 26.5° N (dye fraction). Same color coding as in (a). Overlaid are estimates based on neodymium composition ε_{Nd} from **?** (black triangle for PI, red triangle for LGM).

AMOC

220   The maximum strength of the NADW cell at 26.5° N, which defines the AMOC strength, varies in our PI ensemble between 18.3 and 24.8 Sv (ensemble median is 20.0 Sv) and is located at a depth slightly deeper than 1000 m (see profile of the AMOC at 26.5° N in Fig. 4a). From measurements of the RAPID array at the same latitude for the years 2004 to 2017, the strength of the AMOC has been estimated to be 17.0 ± 4.4 Sv (**??**). The strength of the Antarctic Bottom Water (AABW) cell at 26.5° N varies between 0.4 and 2.5 Sv for the PI ensemble.

225   For the LGM, the spread of the AMOC strength is much larger, showing values between 14.7 and 26.3 Sv, with an ensemble median of 16.8 Sv. Except for simulation D1.2, all runs show a shallower and slightly weaker AMOC cell during the LGM than for their PI counterpart. The vertical extent of the NADW cell, for which the lower boundary is defined as the depth below 2000 m where the AMOC strength equals zero, becomes shallower by 250 m to 450 m for almost all individual ensemble members. However, both the spread of the maximum strength of the NADW cell as well as that of the depth of its lower margin
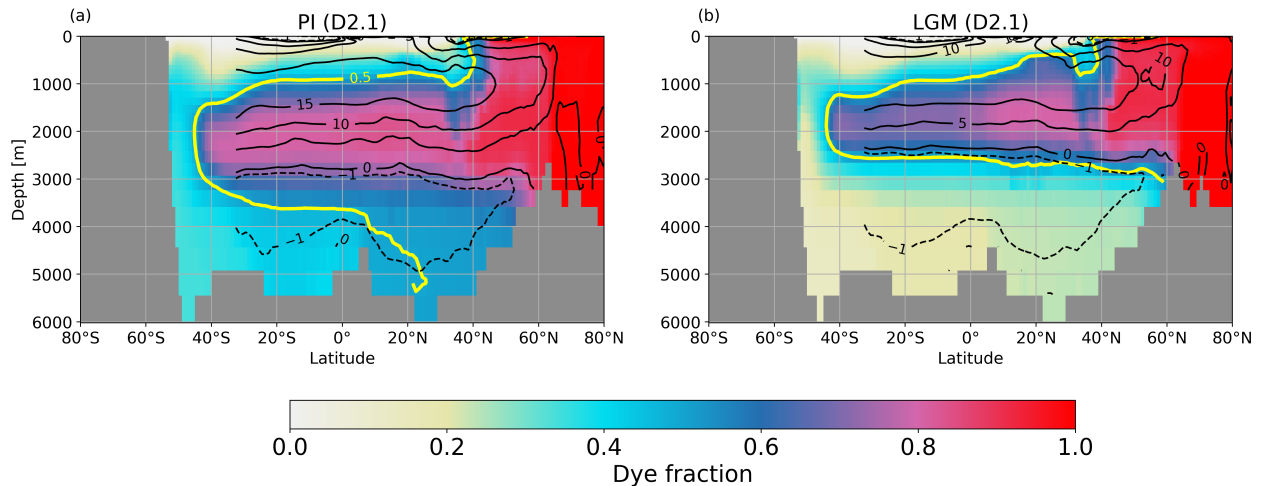
Figure 5. Atlantic section of the zonal mean dye fraction for (a) PI and (b) LGM for one ensemble member (D2.1). Overlaid are contour lines of the AMOC strength (black lines at -1, 0, 5, 10, 15 Sv) and one contour line of the dye fraction (yellow line = 0.5 as indicator of the boundary between NADW and AABW)

230   are about twice as large for the LGM as compared to the PI simulations. The prescribed vertical background mixing in the ocean has a very large effect on the AMOC profile, as can be seen from comparing simulations D1.2, D1.1 and D1.3 (see Fig. A3a). Lower vertical mixing reduces ocean heat transport to high southern latitudes, which results in a substantial cooling (2.4 K colder LGM near surface air temperatures south of 60°S in D1.3 compared to D1.1). This enhances sea-ice formation and thus brine release. For the LGM, the integrated brine release in locations with a positive net sea-ice formation in the Southern

235   Ocean is 28 % higher in D1.3 compared to D1.1 (calculated from decadal mean data), resulting in saltier and denser AABW. Glacial NADW becomes colder as well, but also fresher. Thus, the effective change in density is much smaller than in the south, similar to the findings of Klockmann et al. (2016). The reduced vertical mixing enables a prolonged preservation of the density excess of AABW compared to NADW on its path towards the deep North Atlantic. The consequence is a weakening and shallowing of the NADW cell and an enhanced presence of AABW (see Fig. A3b). Stronger vertical mixing has the opposite

240   effect and leads to a LGM AMOC that is even stronger and deeper than its PI counterpart. Overall, the effect of changes in vertical mixing on the AMOC is larger for the LGM than for PI.

    ? has suggested that the reduced shelf area during LGM lead to stronger tides. **?** applied a tidal model and reports an enhanced energy supply from tides to the internal wave field (1.8 to 3 times higher for LGM than at present, depending on the ice sheet geometries). As we used a time-constant background mixing in our simulations, this effect is not included.

245   For the PMIP4 ensemble, most LGM simulations show a weak deepening and a substantial strengthening of the AMOC (Fig. 4b). This is in contrast to estimates based on proxy data that indicate a shallowing of the AMOC core and a reduction of the circulation strength (e.g **?**), in line with our results.
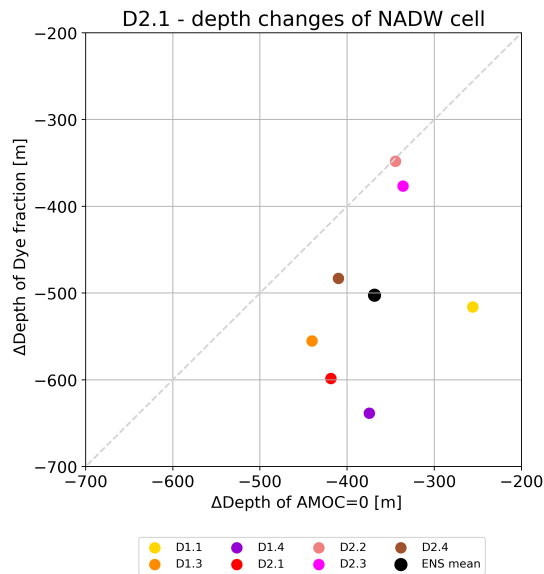
Figure 6. Depth changes between LGM and PI of the dye fraction for the concentration being found for AMOC=0 in PI versus that of AMOC=0 at 26.5° N. Ensemble members and ensemble mean are shown (see legend). D1.2 has been excluded from this analysis (see text). Light-grey dashed line indicates the 1:1 depth change for orientation.

For the assessment of the past AMOC changes, we analyse changes of the dye tracer, which indicates the relative contribution of the water masses originating from the surface of the North Atlantic and Arctic. A decreasing dye fraction reflects larger
250 contribution of water which originates from other source regions, which in the Atlantic below 2000 m is primarily AABW. The dye fraction at 26.5° N shows the core of NADW for PI at depths between 1500 and 3000 m (Fig. 4c). The depth of 3000 m corresponds to the lower margin of the AMOC cell. Below 3500 m, the intrusion of AABW becomes visible by the thick layer of water that consists of a mix of NADW and AABW. For the LGM, the core of the NADW lies shallower and has a reduced vertical extent. The deep layers are dominated by AABW. Estimated changes of the NADW distribution from proxy data show
255 a qualitatively similar pattern (**???**). Note, that the reconstruction of the data by **?** is based on neodymium isotopes, which might underestimate changes of NADW at the LGM due to their source being at the continental slope (**?**), unlike other proxies and our dye tracer, which have their source solely at the surface. Reduced vertical mixing leads to stronger differences in the dye profile at 26.5° N between LGM and PI (see Fig. A3b) in line with the AMOC changes.

Figure 5 illustrates the distribution of the dye fraction and the location and strength of the cells of NADW and AABW at
260 the PI and the LGM for one ensemble member (D2.1). In agreement with the shallowing of the lower boundary of the NADW cell at the LGM, the vertical extension of the dye fraction higher than 0.5 is limited to the upper 2500-3000 m. Qualitatively, the shift of the distribution of water masses between PI and LGM in our ensemble follows the changes derived from proxy data (**????**). However, quantitatively, the change of the AMOC geometry is different from the change in the spatial pattern of the dye fraction. If the lower boundary of the NADW cell is confined by AMOC=0, a dye fraction of about 0.5 is found

at a very similar depth at the LGM. For the PI, the dye fraction at AMOC=0 is much higher (around 0.7) and NADW is the dominant water mass in the deep Atlantic north of 20° N. Our dye fraction provides the opportunity to compare simulated depth shifts of the lower boundary of the AMOC cell to changes in the location of NADW identified by the dye fraction (Fig. 6). As already apparent from D2.1 in Fig. 5, almost all ensemble members show that the shallowing of the dye fraction for the LGM is more pronounced than the shallowing of the NADW cell. Ensemble member D1.2, in which the AABW cell does not extend to 26.5° N, has been excluded from this analysis. For the ensemble mean, the depth change of the water mass boundary indicated by the dye fraction is about 35 % larger than that for the AMOC cell boundary. Note that the dye fraction has no methodological uncertainty and no potential variations in the source function as is the case for proxy data (**???**). The simulated temporal and spatial variations of the dye fraction at AMOC=0 are a result of water mass mixing intensity and emphasize how complicated a straightforward assessment of the AMOC geometry is based on proxy data (see a further discussion in Appendix A5 and Fig. A4). The simulated difference provides therefore a cautionary note for a quantitative validation of AMOC changes with proxy-derived changes in water mass boundaries.

Ice sheets

The simulated Laurentide ice sheet for the LGM has a similar size as in the GLAC-1D reconstructions (Fig. 7, **??**) and ICE-6G (**?**), as shown in Fig. 7. Similar to other studies (**??**), the largest differences occur at the south-eastern margin, where the reconstructions extend further south than the Laurentide ice sheet in the simulations. Moreover, the simulated Laurentide ice sheet shows a clear two-dome structure - one dome covering the Cordilleran (western Laurentide) ice sheet and the second, more prominent dome, covering the eastern Laurentide. The latter is not distinctly visible in the reconstructions. However, the reconstructions exhibit considerable uncertainties, especially in the thickness distribution. Differences in ice thickness between the modelled Laurentide ice sheet and reconstructions are most prominent in the Hudson Bay and Mackenzie areas. Both regions frequently exhibit Heinrich-event (HE) like surge events (e.g. **???**) in our model, which will be discussed in more detail in Section 4.1. The impression that the Labrador Sea is covered by an ice shelf in our simulations stems from the fact that we average over periods with HE-like surge events, during which a temporary ice shelf forms (Fig. 7a, e, and m), and more frequent periods without an ice shelf in the central Labrador Sea. The model simulates a Fennoscandian ice sheet that is in good agreement with the reconstructions with differences restricted to the eastern part of the Fennoscandian ice sheet, where it extends further east in the simulations. All model realisations show an ice mass over Northeast Siberia that is not present in the reconstructions. For the PI, our simulations show a realistic Greenland ice sheet and some smaller ice caps over Svalbard, Novaya Zemlya and other Arctic islands. In general, the size of the ice caps over Norway, Baffin Island and the Rocky Mountains is overestimated. The largest discrepancy to observations occurs in Northeast Siberia, where a considerable ice cap survives the deglaciation, containing between 2.4 –3.2 m sea-level equivalent.

The comparison of simulated ice-sheet size with ice-sheet reconstructions shows larger discrepancies for Antarctica than for the northern hemisphere. Particularly, the marine-based regions of the Filchner-Ronne and Ross ice shelves, where the ice sheet retreated significantly during the deglaciation, are different. Similar results were obtained by previous glacial cycle
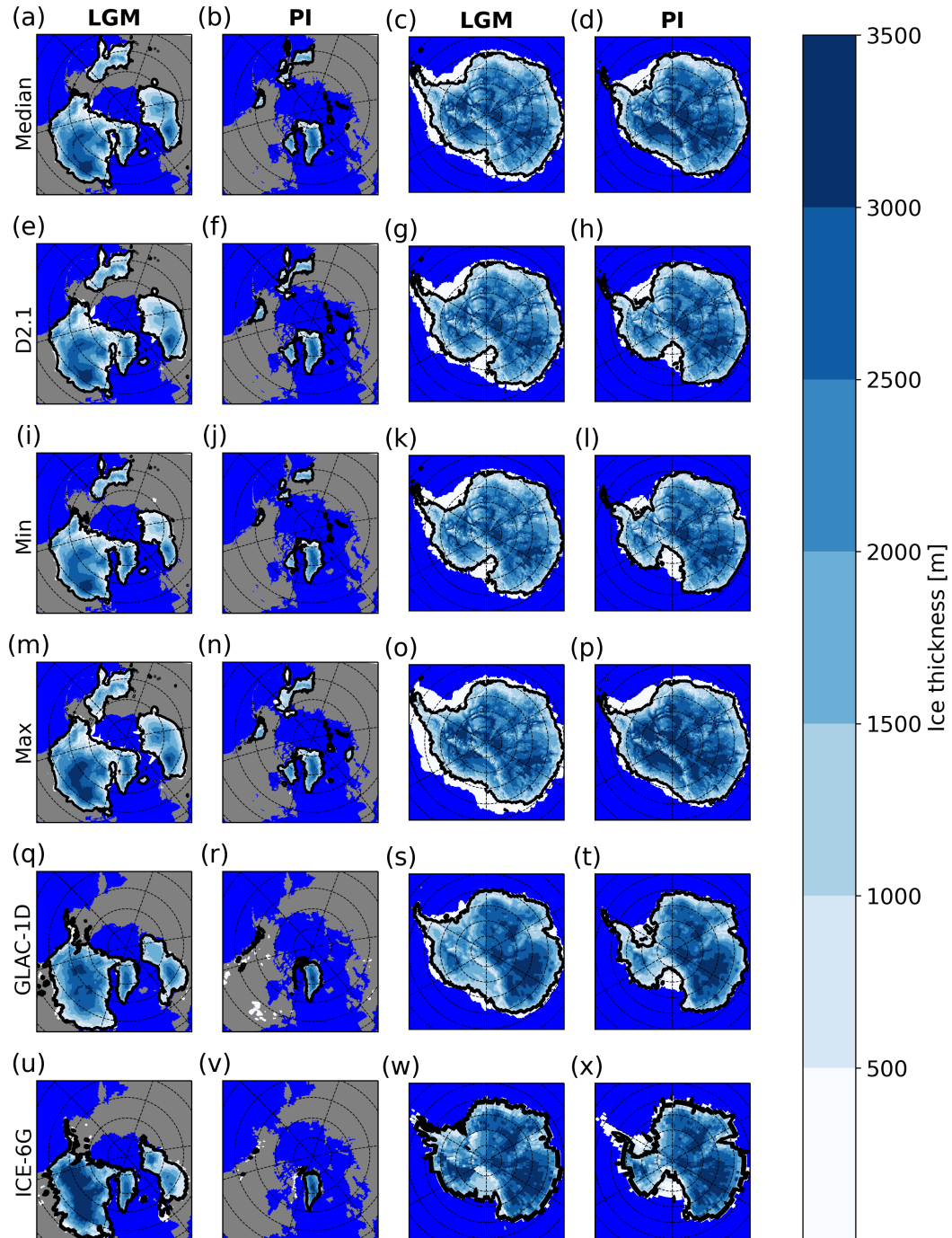
Figure 7. Ice thickness maps for the northern hemisphere and Antarctica. The column title indicates the respective time slice. The rows correspond to (a-d) the ensemble median, (e-h) D2.1, (i-l) the ensemble minimum, (m-p) the ensemble maximum, (q-t) ICE-6G, and (u-x) GLAC-1D. The thick black line indicates the median position of the grounding line. Ice volumes for ice sheets for the LGM and PI are provided in Table A3.

simulations with stand-alone ice sheet models (**????**). All model realisations tend to follow one of the following two scenarios for Antarctica: (i) the ice-sheet advances to the continental shelf edge at the LGM, but does not retreat far enough during the deglaciation; or (ii) the ice-sheet does not advance to the continental shelf edge at the LGM, but retreats to a position in agreement with present-day observations. This indicates that the parameter space for which our model reproduces the advance and retreat pattern of the Antarctic ice sheet could be narrower than for the northern hemispheric counterparts. Therefore, our simulations underline the challenge of successfully simulating the evolution of marine terminating ice sheets over the course of the last deglaciation (**?**)

3.2 Climate evolution over the last deglaciation

In this section, we turn our focus towards the transient climate evolution of the last deglaciation in our model ensemble. We focus on a selection of variables for which proxy data and reconstructions are available and additional variables that give a better physical understanding of the proposed processes.

Near-surface air temperature

Our simulated SATs show an almost continuous warming (Fig. 8a) akin to the trajectory of the PalMod reconstructions and those of **?**. Overall, the simulated warming closely follows the prescribed increase in atmospheric greenhouse gas concentrations with the strongest warming between 17 ka and 10 ka. During the Holocene, our simulations indicate a steady warming trend, which is consistent with the data assimilation product by **?**, but in contrast to the PalMod reconstructions, which indicate a slight cooling trend throughout the Holocene. This discrepancy in the Holocene temperature trend is quite typical. For a detailed discussion of the Holocene temperature conundrum see e.g. **?**.

Sea-surface temperature

Superimposed on the overall warming trend in our simulations are abrupt millennial- and centennial-scale cooling events (Fig. 8f, Fig. 9). This variability is not evident in the proxy based products due to the lower temporal resolution of the reconstructions, which is a consequence of the methodological design and the quality of the underlying proxy data.

The latitudinal distribution of the deglacial ocean surface warming signal is shown in Fig. 9, by comparing the sea-surface temperatures (SSTs) over different latitude bands derived from our ensemble to proxy based estimates. Similar to the global SAT evolution, the ocean surface temperature evolution in the northern extratropics shows a continuous warming throughout the entire simulation, interrupted by several abrupt cooling events. Thereby, the model spread of the transient signal is about 1 K, if the abrupt cooling events are excluded (see Fig. 9). A slow warming trend is present at all latitudes until 17 ka, after which the warming significantly accelerates. In contrast, both proxy based data sets show a temperature minimum around 17 to 16 ka, at the time of H1, followed by rapid deglacial warming which tapers off between 14 and 13 ka.

In the proxy data set, the Younger Dryas cold event peaks between 13 and 12 ka. A similar cooling signal is also modelled in some of the runs (e.g. D1.1, D1.2 and D1.4) albeit with a weaker amplitude than in the reconstructions. In general, the timing
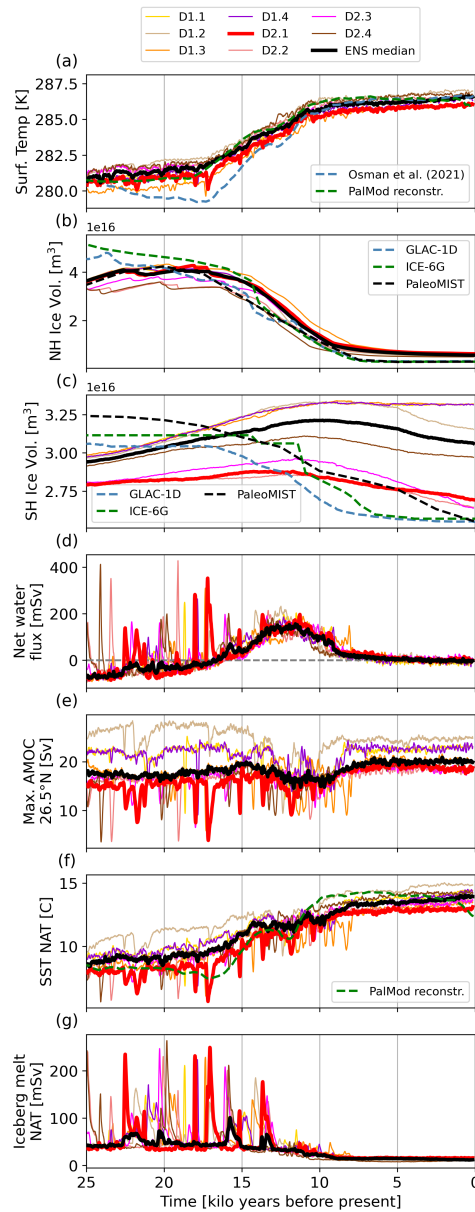
Figure 8. Time series of global mean (a) near-surface air temperature, ice volume in the (b) northern hemisphere and (c) Antarctica, (d) net freshwater flux into the ocean, (e) strength of the AMOC at 26.5° N, (f) average SST of the North Atlantic (north of 30° N) and (g) iceberg meltwater flux into the North Atlantic for the model ensemble. The ensemble median is plotted with a thick black line. Model data shown are 100-year running means for climate model variables. Ice volume data are derived from snap shots 50 yr apart. Observational estimates are plotted in the time resolution given by the original data sets. The data from the PalMod reconstructions are anomalies relative to PI. They were transformed into absolute values by adding the last value from the ensemble median.

of the occurrence of individual abrupt events, however, varies between the model runs. From 12 ka onward, all curves show a strong warming until the beginning of the Holocene. Hereby, the modelled warming rates are lower than suggested by the proxy data. During the Holocene, the model runs indicate a weak warming trend, in accordance with the **?** estimate.

In the tropics, the model simulations show a glacial cooling amplitude that is sandwiched by the proxy data, whereupon the PalMod reconstructions indicate less cold SSTs and the reanalysis of **?** indicates cooler SSTs. The onset of the deglacial warming is overall delayed by approximately 1 kyr. The simulated warming signal here is much smoother and the millennial-scale variability seen in the northern hemisphere extratropics is much reduced. While this is in accordance with the reconstructions from PalMod, the **?** reanalysis shows a temporal variability rather similar to the northern extratropics. In addition, during the early phase of the deglacial warming, the model ensemble is slightly colder than the uncertainty range from the PalMod reconstructions.

In the southern hemisphere extratropics, the model simulations agree very well with the reanalysis data by **?** and lie within the uncertainty range of the PalMod proxy data. All data sets show a slight warming trend through the glacial period. The deglacial warming starts between 18 and 17 ka. The amplitude of the millennial scale variability is relatively small compared to the other latitude bands. After 11 ka the mean SST in this latitude belt remains stable, which is also indicated by the proxy data (Fig. 9c).

Ice sheets

At around 25 ka, the simulated northern hemispheric ice volume is lower than the ice volume in the ICE-6G (**?**) and GLAC-1D (**??**) reconstructions (Fig. 8b), but matches well with the estimate from the more recent PaleoMIST (**?**) reconstruction. The discrepancy in ice volume between the simulated and the ICE-6G and GLAC-1D ice sheets originates from the overall thinner simulated ice sheets at the beginning of the simulation, primarily in the central ice-sheet regions. The maximum ice volume for ICE-6G and GLAC-1D occurs around 25 ka, followed by a steady ice-volume decrease. The same time period in our simulations is characterised by an ice volume gain, as is also shown by the PaleoMIST reconstruction. The long-term mass gain is only interrupted by repeated surge events. The growth of the ice sheet is directly related to the continuously low greenhouse gas concentrations prior to 21 ka, resulting in rather cold climate conditions (Fig. 8a). In our simulations and the PaleoMIST reconstructions, the simulated maximum ice volume is typically reached at around 18 ka. At this time, the GLAC-1D reconstruction lies also well within our ensemble spread, whereas the ICE-6G reconstruction indicates larger ice volumes than all model realisations. After 18 ka, ice-sheet volume slowly decreases in our simulations, transitioning into the last deglaciation with the strongest ice-volume loss occurring between 14 and 10 ka. Ice-volume loss tapers off markedly after 8 ka. At PI, our simulations overestimate ice volume in the northern hemisphere by 42-47% in comparison to the reconstructions. The main reason for this is the slow melting of the additional ice caps present in eastern Siberia and over Baffin island (Fig. 7, second column).

Ocean mixing has a considerable effect on the timing and duration of the deglaciation. Enhanced background mixing in D1.2 leads to a faster decay of the northern hemisphere ice sheets compared to D1.1, reduced mixing on the other side delays the
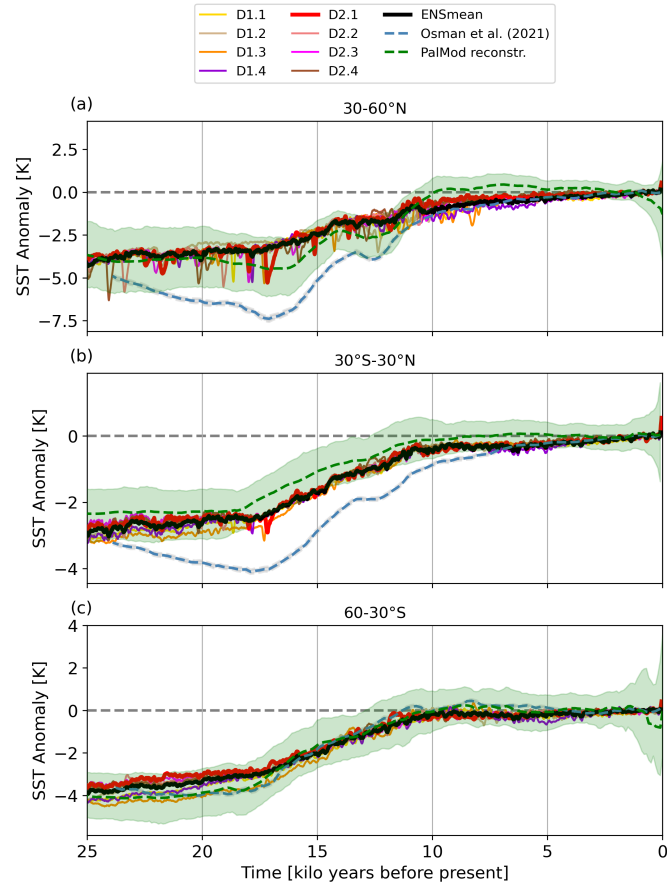
Figure 9. Time series of SST anomalies relative to the PI period for different latitude belts: (a) for the northern mid-latitudes, (b) the tropics, and (c) for the southern mid-latitudes. Beside our model ensemble, SSTs from the PalMod reconstructions (green; see Appendix A2) and the reanalysis of **?**, blue are shown (see also Fig.2). The shading indicates uncertainty estimates, as derived by the PalMod reconstructions. All data were regridded onto a 0.5° grid before averaging over each latitude band. Note, that the data frequency differs: **?** provide 200-year means of annual SSTs, the PalMod reconstructions provide data with a temporal resolution of 100 years and our ensemble is shown as 100-year running means calculated from decadal mean data.

decay (see Fig. 8b and d). Higher vertical mixing enhances Atlantic heat transport in the North Atlantic (not shown), which in turn leads to a warmer climate (compare experiments D1.3, D1.1 and D1.2 in Fig. A1) favouring ice sheet melt.

365 As for the northern hemisphere, the simulated ice volume in the southern hemisphere is lower than indicated by the ice sheet reconstructions at the beginning of the simulation at 25 ka (see Fig. 8c). While all reconstruction show either constant ice volume or a slight decrease after 25 ka, our simulations exhibit an ice-volume gain until 12–10 ka. Most of our model simulations show an ice-volume decrease only afterwards. However, the magnitude of the ice-volume loss is not large enough over the remaining simulation period, resulting in an Antarctic ice sheet that is too extensive and for which the grounding line positions

370 are too advanced for PI. Overall, the simulated and reconstructed ice-volume evolution does not match with reconstructions as well as for the northern hemisphere. Especially, the advance and retreat magnitudes of the simulated Antarctic ice sheet are underestimated and do not show enough fidelity. As the signals arising from changes in the Antarctic ice sheet are rather small, they did not have an obvious effect on the simulated climate signals during the deglaciation.

Net freshwater flux into ocean

375 The net water flux into the ocean (Fig. 8d), which on centennial mean time scales is almost identical to the time derivative of the mass of the terrestrial ice sheets, aligns with the growth of the northern hemisphere ice sheets during the last part of the glacial. This growth is interrupted by strong discharge events on millennial time scales. From 17 ka onward, the net water flux remains largely positive as a result of the ongoing decay of the ice sheets, with melt rates (direct meltwater discharge as well as melting ice bergs) larger than 0.1 Sv between 14 and 10 ka. At the end of the deglaciation, around 8 ka, the ice sheet mass

380 loss and hence the net water flux reduces drastically and stays relatively constant through the entire Holocene.

  From sea level reconstructions at Barbados, **?** showed the existence of two meltwater pulses. For the first one, MWP1A, **?** estimated meltrates larger than 0.46 Sv for more than 300 years. MWP1A coincides with the rather warm period of the BA. Ice-sheet reconstructions such as ICE-6G and GLAC-1D suggest that most of the meltwater was discharged into the North Atlantic or Arctic ocean. None of our coupled simulations produces an amount of meltwater similar in magnitude to MWP1A

385 around 14 ka . However, meltwater pulses close to 0.4 Sv do occur in our simulations during some of the abrupt events. The existence of the second meltwater pulse, MWP1B, before 11 ka was questioned by e.g. **?** based on sea level reconstructions from the tropical Pacific. It is not simulated by our model either.

AMOC

The time series of the maximal strength of the AMOC cell at 26.5° N shows marked millennial-scale variability during the

390 glacial period (Fig. 8e). The spread between the ensemble members is considerable. Most simulations show a strengthening of the AMOC from the glacial to the late Holocene. However, there are also simulations with a rather small change in the AMOC between LGM and PI and one simulation (D1.2) with a stronger AMOC at the LGM than at the PI. During the peak of the deglaciation, all simulations show a weakening of the AMOC, which we explain as the response to meltwater hosing, enhancing vertical stability and reducing the ventilation of the deep water masses. The slow warming in response to rising

GHG concentrations further amplifies vertical stability. Except for short periods of time, the model AMOC is always in a strong mode.

4 Abrupt events

The transient climate evolution of the past 25 ka is interrupted by several abrupt events. For each of our ensemble members, these abrupt events occur at very different times during the glacial and the deglaciation. Here, we focus on the deglacial key events, which are related to changes in the AMOC. To examine the drivers of the abrupt events, we first focus on the simulation D2.1. Figure 10b shows the time evolution of the AMOC and the dye fraction over depth at 26.5° N. The overall trend of a strengthening and deepening of the AMOC cell from the glacial to the Holocene is interrupted by numerous abrupt events, which are accompanied by strong signals in the dye fraction and indicate water mass displacements throughout the whole water column (see also Fig. A4). A close relationship between changes in the net fresh water flux (Fig. 10a) and variations in AMOC and the dye fraction profile is visible.

In the following we will examine individual abrupt events and discuss the underlying mechanisms. Based on our simulations, we can distinguish between three different mechanisms behind the simulated abrupt cold events: HE-like surges from the northern hemispheric ice sheets, and events that are triggered by changes in the Arctic net-freshwater budget or a river rerouting over North America.

4.1 Drivers of abrupt climate events during the last deglaciation

HE-like surge events

The first deglacial meltwater peak in D2.1 occurs around 18.0 ka (event 1 in Fig. 10a). The snapshot maps (see Fig. 11a) show that the event at this time is caused by a surge event from the Fennoscandian ice sheet, with massive iceberg discharge into the Norwegian Sea. This enhances iceberg melt in the Nordic Seas and the North Atlantic. The meltwater reduces surface salinity, suppresses deep convection and consequently leads to a weakening of the AMOC and an upward shift of the margin between AABW and NADW (Fig. 10b). These changes are accompanied by a surface cooling in the North Atlantic (see Figs. 10c and 8f). Note that the SST cooling in the subpolar and the subtropical North Atlantic associated with AMOC weakening events is of similar magnitude during the glacial and early deglaciation (Fig. 10c). The glacial temperature at the subpolar location is already rather close to freezing point, which very effectively limits the potential amplitude of any cooling signal at this location.

The next meltwater peak, occurring around 17.22 ka (marked as 2 and 3 in Fig. 10a), is caused by surges from the Laurentide ice sheet (Fig. 11b). The event consists of two almost synchronous surges from two source regions of the Laurentide ice sheet. First, a surge in the western part of the Laurentide towards the Arctic occurs. While this surge slows down, another surge takes place from the eastern Laurentide through Hudson Strait (Fig. 11c). This abrupt event is rather strong with a weakening of the AMOC down to 3.9 Sv at 17.2 ka (as indicated in the 100 yr means in Figs. 10b and 8e). As a result, the margin between the NADW and the AABW cells shifts upward by approx. 800 m. The depth of the 70% NADW dye fraction moves upward and
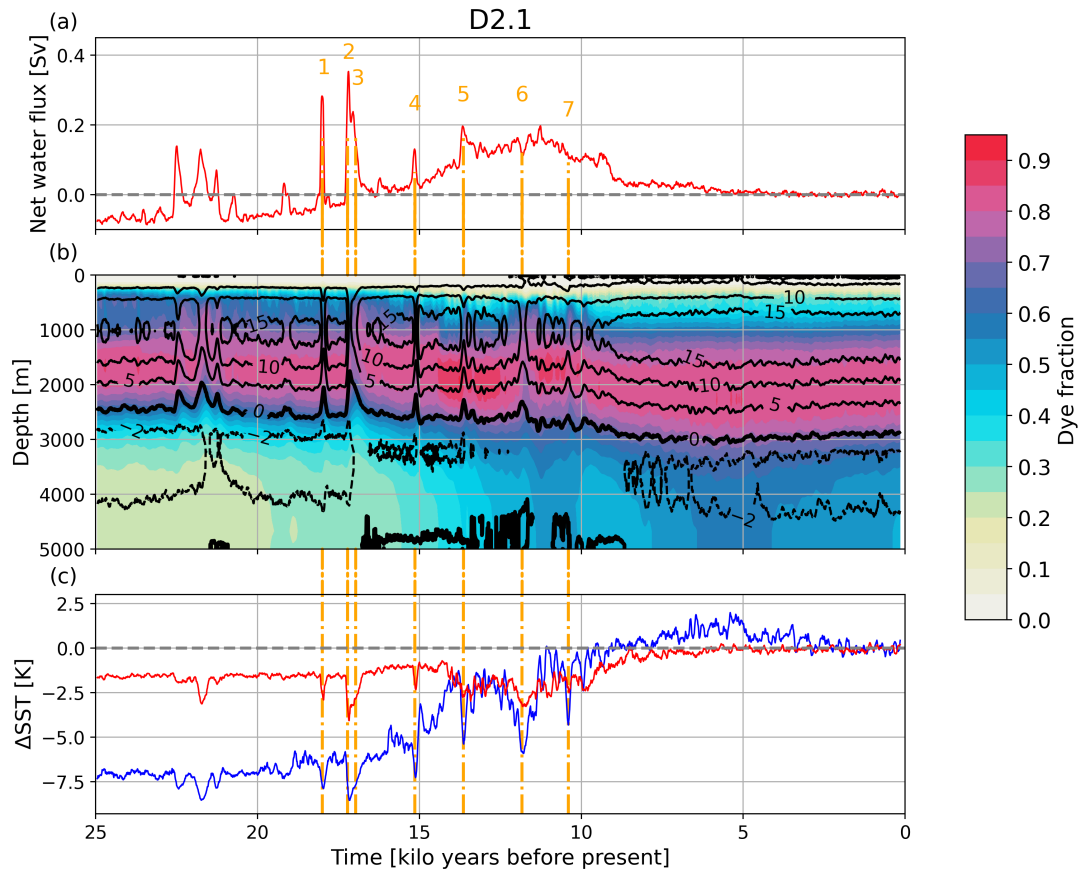
Figure 10. (a) Time series of the global freshwater input into the ocean, (b) a time-depth plot of the AMOC at 26.5° N superimposed on the zonally averaged fraction of water originating from the surface of the North Atlantic and Arctic, and (c) SST anomaly time series at 54° N 30° W in the subpolar (blue) and 38° N 46° W in the subtropical (red) North Atlantic for ensemble member D2.1. Orange dashed-dotted lines and orange numbers in (a) mark specific AMOC weakening/ North Atlantic cooling events discussed in the text. Contour lines in (b) are at -2, 0, 5, 10, and 15 Sv. The thick black line between 2000-3000 m indicates the lower boundary of the NADW cell (AMOC = 0 Sv). Data shown are 100-year running means.

reaches a maximal uplift of about 400 m 200 years later. The two surges combined discharge a water equivalent of almost 8 m of global sea level within 450 years. This is within the previously reported range for HEs of 2–20 m over a time period of 500 years (**???**) .

The next event, at approximately 15.14 ka (marked as 4 in Fig. 10a), is again caused by a discharge event from the Fennoscandian ice sheet into the Norwegian Sea (Fig. 11d). It is followed by the last big iceberg discharge event around 13.64 ka (event 5 in Fig. 10a) from the eastern Laurentide ice sheet through Hudson Strait (see Fig. 11e). As the deglacial warming is already ongoing during these two events and the temperature at the subpolar location is now well above the freezing point, the SST cooling signals in the subpolar location are now stronger than in the subtropics, similar to the responses known from typical PI hosing experiments (e.g., **???**).

Events not caused by ice surges

After 13.64 ka, the North Atlantic in D2.1 shows two more distinct SST cooling events (marked as 6 and 7 in Fig. 10). The first of these events reaches a temperature minimum around 11.83 ka and the other one at 10.4 ka in simulation D2.1 (Fig. 10c). They coincide with a significant decrease in the maximum AMOC strength (Fig. 10b). But, unlike the previous events, they cannot directly be associated with an abrupt increase of the total amount of meltwater and/or iceberg discharge from the Laurentide or Fennoscandian ice sheets (Fig. 10a).

Sign shift in the Arctic net-freshwater balance

The first of these two cold events takes place during the peak of the deglaciation (event 6 in Fig. 10a). During this time, the Laurentide and Fennoscandian ice sheets experience significant mass loss in response to the increase in global temperatures and summer insolation. This is indicated by an increase in global meltwater release (Figure 10a), which is most pronounced in the Arctic (Fig. 12b). This meltwater input into the Arctic leads to a regime shift in the net freshwater budget of the Arctic ocean. This quantity is defined as the balance between the meteoric freshwater input (river runoff, precipitation and iceberg melt minus evaporation) and the export of sea ice from the Arctic into the adjacent seas, and represents a measure for the integrated net freezing rate of Arctic sea ice and the associated brine release. During the glacial, the Arctic sea-ice export and thus the brine release dominates over the meteoric freshwater input. Hence, the water leaving the Arctic has a higher salinity and colder temperatures and is therefore denser than the inflowing water of Atlantic origin. As a consequence, it contributes to the formation of NADW. Due to the increase in meltwater input from the Laurentide ice sheet into the Arctic ocean, the net freshwater budget becomes positive for the first time at about 12.47 ka. This means that the Arctic transitions from a state with an effective net freshwater loss due to sea-ice formation and export to a state with a positive net freshwater budget (Fig. 12b). While this transition occurs rather gradual and takes until about 11.78 ka to be completed in D2.1, it allows for an abrupt decrease in the surface salinity in the Arctic, as the positive net freshwater input allows for a halocline to develop. This stabilizes the stratification in the Arctic and suppresses deep convection in the Arctic. Furthermore, the water leaving the Arctic is now fresher and less dense than the inflowing water. The resulting reorganisation of the NADW formation leads to a decrease in AMOC strength. At first the AMOC weakening is rather gradual and overlaid by large centennial-scale variability.
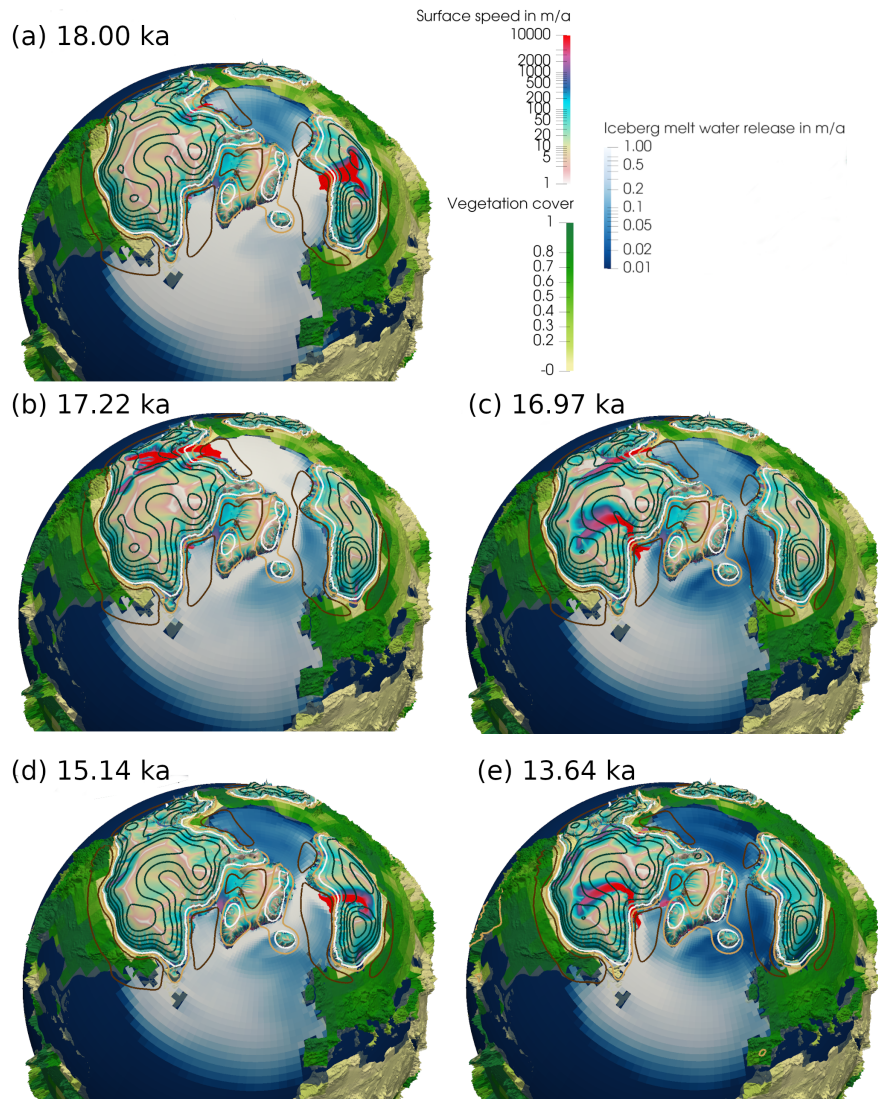
Figure 11. Snapshots of different surge events from the northern hemisphere ice sheets during the last deglaciation for simulation D2.1. The movie of the entire deglaciation is available under https://doi.org/10.5446/69659 (**?**). Colours on the ice sheets indicate the surface speed, colours on land maximum vegetation cover and colours in the ocean the amount of iceberg meltwater release. Isolines indicate the vertical displacement of the bedrock relative to the end of the simulation. Black isolines indicate depressed bedrock, brown isolines elevated bedrock as compared to PI. No change is indicated by a white isoline. The spacing between individual contours is 100 m with the exception of the $\pm$ 50 m contour.

The gradual decrease in Arctic sea-ice export starting at about 12.0 ka results in a further increase in the net freshwater budget and ultimately leads to an abrupt weakening of the AMOC (Fig. 12c).

The overall increase in sea level and the retreat of the ice sheets results in the opening of the Bering Strait as well as of the Barents Sea opening at about 11.37 and 11.18 ka, respectively. The opening of Bering Strait leads to a considerable reduction of Arctic sea-ice volume (about 20%) and results in a net export of freshwater into the Pacific (not shown). The opening of the Barents Sea further allows for additional sea-ice export to the Nordic Seas (about 20%). Hence, the opening of both straits ultimately increases the surface salinity in the Arctic, which decreases the stable stratification, enhances the deep water formation, and allows for an increase of the AMOC strength to nearly to pre-event values. Note, that the AMOC recovers slightly before the abrupt salinity increase in the Arctic in response to the opening of the Bering Strait. This increase can likely be attributed to a substantial centennial to millennial variability of the AMOC (see Fig. 12a and 12c).

It is noteworthy that the freshwater input into the Nordic Seas increases rather rapidly around the time of the opening of the Barents Sea Opening at 11.18 ka. This increase is associated with a redirection of meltwater from the southern margin of the Fennoscandian ice sheet. Relatively small changes in the land–sea mask and ice-sheet margin allow for a redirection of these waters from the North Sea towards the northeast into the White Sea and eventually into the Barents Sea, causing an abrupt increase in the freshwater input into the Nordic Seas (see Fig. 12b) and reduction in Nordic Seas surface salinity.

Changes in river routing

The second of the non-surge induced cooling events (about 10.4 ka; event 7 in Fig. 10) is driven by a redirection of meltwater from the Laurentide ice sheet. At this time, much of the meltwater from the Laurentide ice sheet is routed through the St. Lawrence or Mackenzie Rivers and ends its path either in the North Atlantic or Arctic, respectively. The paths of the two rivers follow the southern edge of the Laurentide ice sheet and are separated by a drainage divide located northwest of today's Great Slave Lake (Fig. 13). At about 10.49 ka, the continued retreat of the northwestern part of the Laurentide ice sheet in conjunction with changes in the land topography through glacial isostatic adjustment, allows for the Mackenzie drainage basin to extend much further southeast, all the way towards the Great Lakes (Fig. 13). This rerouting leads to a redirection of approximately 0.08 Sv of meltwater from St. Lawrence River to the Mackenzie River and results in an abrupt increase in meltwater discharge into the Arctic (Fig. 12b). The freshwater is transported through the coastal boundary currents of the Arctic Ocean towards the deep-water formation sites in the Greenland and Labrador Seas, where it leads to a reduction of the NADW formation and thereby a weakening of the AMOC.

The enhanced discharge of meltwater into the Arctic lasts until about 9.41 ka. At this time, the Laurentide ice sheet collapses and splits into two small ice sheets on Baffin Island and on southeast Canada. The associated changes in sea level and glacial isostatic adjustment lead to the opening of the Hudson Bay (Fig. 12) and allow for a rerouting of water into the Hudson Bay (Fig. 13). A consequence of the ice-sheet collapse is a short increase in the release of icebergs and their melt into the North Atlantic (Fig. 8g). In response to these changes in the river routing, the AMOC recovers and slowly increases towards its modern strength.
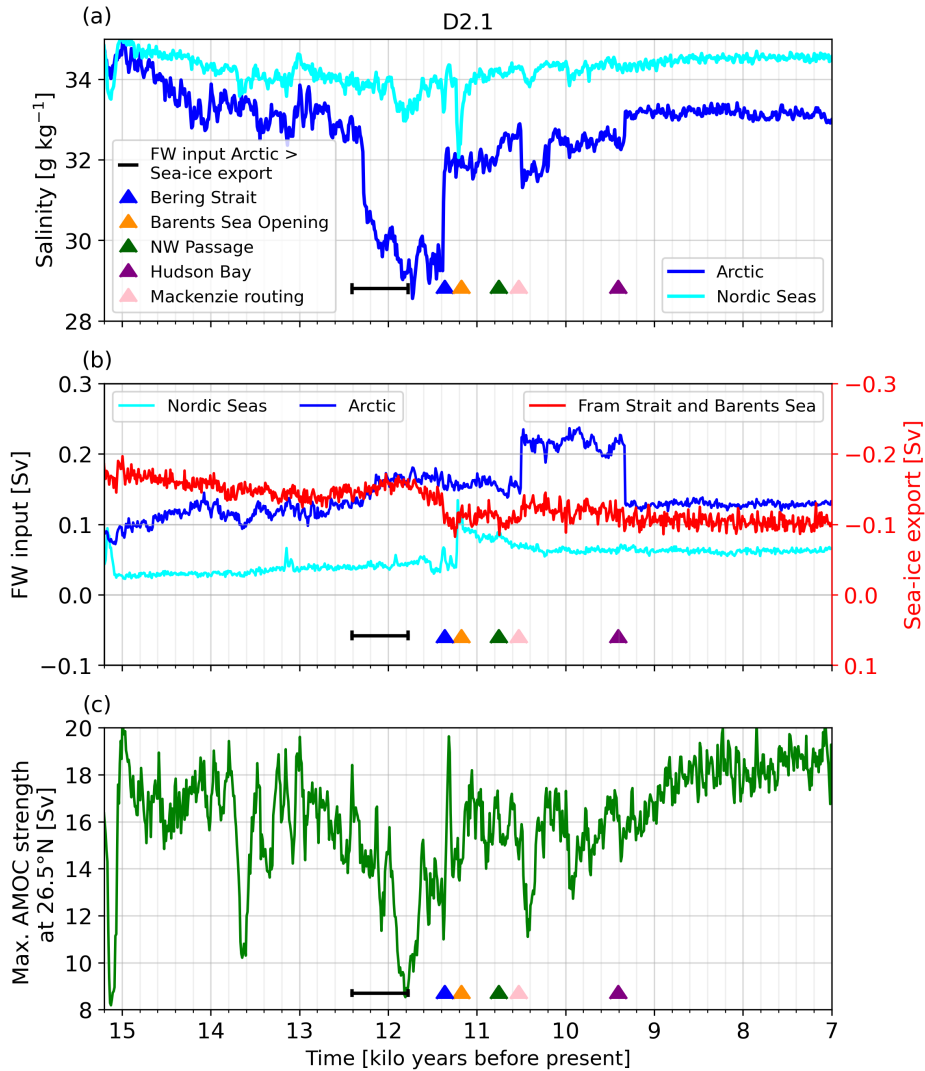
Figure 12. Time series of the (a) surface salinity in the Arctic (blue) and Nordic Seas (cyan), (b) the freshwater input into the Arctic (blue) and Nordic Seas (cyan), both derived from precipitation minus evaporation, river runoff and iceberg melting as well as the Arctic sea-ice export through the Fram Strait and Barents Sea Opening (red; right axis) in simulation D2.1. (c) Time series of the maximum AMOC strength, as presented in Fig. 8d. All data are shown as decadal means. The black bar indicates the sign shifts of the Arctic freshwater budget, whereby the time range shows when the decadal surface freshwater budget of the Arctic becomes for the first time positive and the last time negative. The triangles mark the opening of the major Arctic Ocean gateways, namely the Bering Strait (blue), the Barents Sea Opening (orange), the Northwest Passage (green) and the opening of the Hudson Bay (purple). The change in river routing that allows for enhanced freshwater input through the Mackenzie river into the Arctic ocean is indicated in pink.
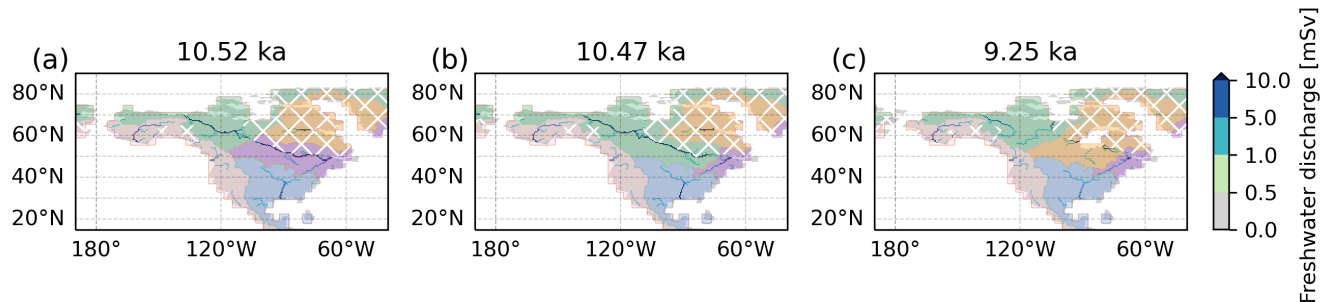
Figure 13. Snapshots of the river discharge and their catchments for a time slice before and after the change in the river routing that triggers the 10.4 ka cooling event in D2.1 and after the Hudson Bay opening in the ocean model. Shown is the river discharge through the main rivers (colorbar) over North America at (a) 10.52 ka, (b) 10.47 ka, and (c) 9.25 ka together with the main catchment areas, indicated by the colored overlays. Note that several catchments are combined in one color: shown are all catchments that discharge into the Arctic (green), the Baffin Bay and Labrador Sea (orange), the North Atlantic and Nordic Seas (purple), the southern North Atlantic (blue) and the Pacific (pink). The gray background shading marks the land–sea mask on the ocean model grid. White hatching marks the glacier mask, as obtained from the ice-sheet model.

Table 2. Timing of the opening of the Arctic Straits, and the change in the river routing favoring enhanced discharge through Mackenzie river in ka. All events are marked by triangles and the black bar in Fig. 12. Values for ICE-6G_P3 and GLAC-1D_P3 are taken from transient deglacial simulations with prescribed ICE-6G and GLAC-1D ice-sheet reconstructions, respectively (see ?). Shading indicates that the opening is more than 1000 years earlier (red) or later (blue) than the range given by proxy evidence.

Name	Bering Strait	Barents Sea Opening	Canadian Archipelago	Hudson Bay	Arctic freshwater	Mackenzie routing
D1.1	8.46	11.87	11.61	9.27	14.47-13.65	10.50
D1.2	8.91	12.15	11.93	10.86	14.91-14.05	11.11
D1.3	7.82	10.86	10.75	8.16	13.81-12.81	10.57
D1.4	8.43	11.58	11.69	9.19	14.52-13.93	9.73
D2.1	11.37	11.18	10.76	9.41	12.41-11.78	10.51
D2.2	16.11	12.47	12.06	9.89	14.27-11.99	10.71
D2.3	12.28	11.67	11.72	9.77	12.90-12.34	10.38
D2.4	12.69	12.75	12.96	10.84	14.46-13.39	11.73
ICE-6G_P3 [a]	11.13	14.03	10.33	8.68	16.09-14.77	12.62
GLAC-1D_P3 [a]	11.19	15.08	10.43	8.44	15.86-13.38	11.56
Proxy evidence	10.30-13.10 [b]	16.0-15.0; 12.0 [c]	8.5-7.5 [d]	8.6-8.2 [e]	-	-

[a] **?**, [b] **?????**, [c] **??**, [d] **??**, [e] **?**

4.2 Abrupt events in the ensemble

In this subsection we discuss, how robust the mechanisms that we have found in the previous subsection are. For this we are now discussing the entire ensemble. All ensemble members show abrupt millennial scale events (see Fig. 8) similar to the events presented for D2.1. Abrupt AMOC weakening events lead to a strong cooling in the North Atlantic SST of several Kelvin. Many of these events also show large pulses of iceberg melting in the North Atlantic, indicative of HE-like surge events. Hence, we will distinguish in the following between HE-like surge events, abrupt events induced by a persistent sign shift in the Arctic net-freshwater balance or changes in the river routing.

Abrupt events due to HE-like surges

HE-like surges are caused by internal variability of the northern hemisphere ice sheets in our model system (**???**), which largely follows the classic binge-purge mechanism suggested by **?**. However, the timing of these events is highly variable as shown by the considerable spread between the ensemble members. As the external forcing (orbital parameters and atmospheric greenhouse gas concentrations and for a subset of our ensemble also the volcanic forcing) is identical in all simulations, it cannot serve as explanation for the difference in the timing of the events. As all asynchronous spin-up simulations started from the same state at 45 ka, model parameters obviously have an effect on the timing of the surge events.

To test the role of initial conditions, two additional sensitivity experiments have been performed. These simulations are identical to D2.1 except for slight differences in the initial fields for the ice sheet and solid earth model. Instead of the 26 ka conditions, we used the ice sheet and solid earth conditions from 27 ka (D2.1.1) and 28 ka (D2.1.2) in the asynchronous spin-up as initial state. Together with D2.1, the simulations D2.1.1 and D2.1.2 thus allow us to investigate the effect of the initial state of the ice sheet on the timing of the surge events. Of our three main surge regions, Hudson Strait tends to show the most regular interval between individual events, suggesting a higher predictability of surge events than the other regions. D2.1.1 and D2.1.2 simulate Hudson Strait surge events that are offset by 1 and 2-kyrs (Fig. 14a), which matches the shift in the initial state of the ice sheets and corroborates a high level of predictability shown in previous studies (**??**). In agreement with these studies, the level of predictability is considerably lower for the surges originating from the western Laurentide ice sheet. For this region, the spread in the timing and strength of the events is much more irregular and the simulated shifts in D2.1, D2.1.1 and D2.1.2 are closer to 1 ky instead of the expected 1 and 2 ky (Fig. 14b) from the initialization. The predictability for our third surge region, the Fennoscandian ice sheet, lies somewhere in between the predictability of the other two surge regions (Fig. 14c). Overall, our sensitivity simulations clearly demonstrate the importance of the initial conditions for the timing of the surge induced abrupt events.

Furthermore, the simulated climate over the ice sheets (especially surface mass balance and surface temperature) has an effect on the timing and frequency of the surge events (**??**). Together with the rather chaotic surge behaviour of the Mackenzie ice stream this further enhances the stochastic contribution in the timing of the surge events. Both, initial conditions and the choice of the model parameters influence the timing of the surge event. In consequence, the exact timing of surge-type variability, as derived from observations, cannot be reproduced by a model with interactive ice sheets.
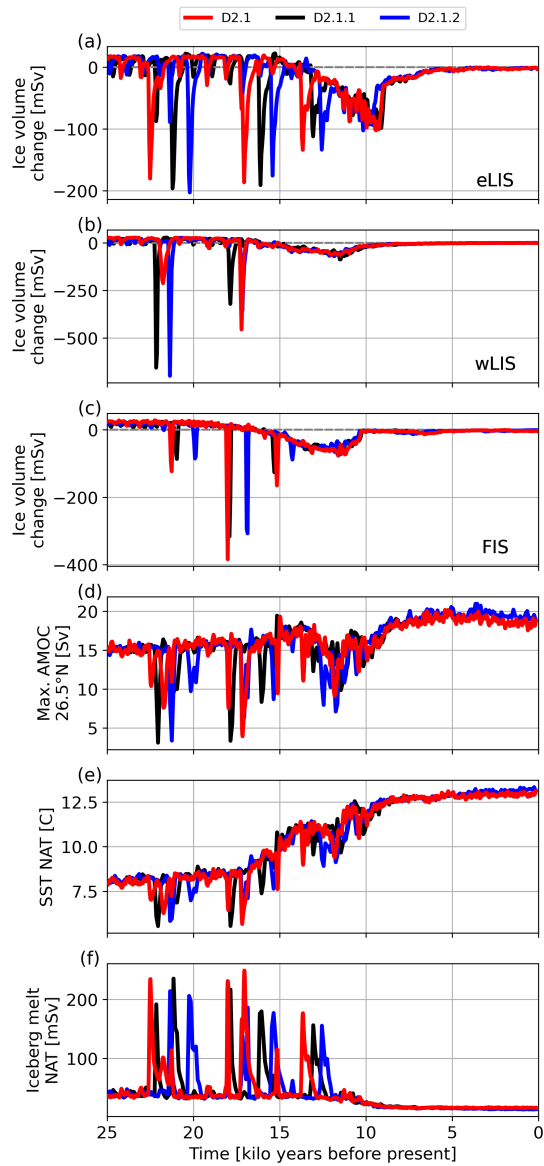
Figure 14. Change in ice volume for the (a) eastern Laurentide (eLIS), the (b) western Laurentide (wLIS), and the (c) Fennoscandian (FIS). (d) shows the strength of the AMOC at $26.5°$ N, (e) the average SST of the North Atlantic, and (f) the iceberg meltwater flux in the North Atlantic for simulations D2.1, D2.1.1 and D2.1.2.

 Late deglacial abrupt events

The last two North Atlantic cooling events in D2.1, which are not associated with the occurrence of HEs, can be identified also in most other ensemble members (Fig. 8e, f). While the timing of the individual events differs between ensemble members, the processes leading to abrupt events in D2.1 are similar in all ensemble members.

Sign shift in the Arctic net freshwater balance

530 In most of our simulations, the onset of the first event not induced by ice-sheet surges is associated with the transition into a regime in which the net freshwater input into the Arctic becomes larger than the sea-ice export to the North Atlantic. This leads, similar to D2.1, in all simulations to the formation of a halocline in the Arctic and a significant reduction in the AMOC strength. However, the timing of the transition towards a positive net freshwater input into the Arctic varies between simulations. Therefore, the timing at which the AMOC strength significantly reduces also differs across ensemble members. For

535 example, D2.2 and D2.3 show weaker AMOC slowdowns and North Atlantic cooling during the onset of this abrupt cooling event than the other simulations. This is likely related to the Bering Strait being open already before the event, at 16.11 ka in D2.2 and 12.28 ka in D2.3 (see Table 2), ultimately influencing the freshwater balance by sea ice export to and the inflow of saltier water from the North Pacific. This is in line with **?**, who showed that the Arctic gateways can have a different impact on the ocean dynamics in the Arctic, depending on whether the Bering Strait or Canadian Archipelago are closed or open. Our

540 findings are also in agreement with findings by **?**, who showed that abrupt AMOC transitions are more likely when the Bering Strait is closed. In accordance with **?**, we find that the simulations that exhibit a late opening of the Bering Strait show stronger variations in the Arctic ocean and AMOC in response to the shift of the sign in the net freshwater balance than the simulations with an early opening.

In our simulations the Bering Strait also plays a pivotal role towards the end of the abrupt event initiated by the changes

545 in the freshwater budget of the Arctic. As shown for D2.1, the opening of the Bering Strait leads to a recovery of the AMOC through an increase in salinity of the Arctic and, thus, a decrease in the vertical stability (see section 4.1). This is the case for all but one of the ensemble members. In line with **?**, who found that the opening of the Bering Strait leads to a substantial salinity increase in the top 50 m of the Arctic ocean, our simulations show a substantial increase in surface salinity for D2.1 (Fig. 12b) and the majority of our simulations (D1.1, D1.2, D1.3, D1.4, D2.3, D2.4, not shown). We find, that part of this increase in

550 surface salinity can be attributed to a net export of freshwater through the Bering Strait into the Pacific (not shown), which is in agreement with findings by **?**. As the timing of the Bering Strait opening varies significantly between simulations, the full recovery of the salinity also varies. For the simulations with a late opening of the Bering Strait (D1.1, D1.2, D1.3, D1.4), the Arctic is able to maintain low surface salinity and thereby its stable halocline over several millennia. This leads to an overall weaker AMOC with substantially higher variability throughout the course of the deglaciation, until the Bering Strait finally

555 opens (see Table 2).

It is noteworthy that the ocean response to an opening/closing of the Bering Strait differs from other studies in some aspects. For example, **?** argue that the opening/closing of the Bering Strait has a substantial impact on the sign of the freshwater budget

in the Arctic. They find that if the Bering Strait is opened under deglacial conditions (15 ka), the Arctic changes from a freshwater sink to a freshwater source. Our simulations do not show such a relationship. Rather, they show a transition from a

560 typical glacial state, where the sea-ice export from the Arctic to the Atlantic is larger than the freshwater input into the Arctic, to a state where the freshwater input is larger. Further, our simulations show that this transition is an inherent transient climate response that occurs in all simulations independent of when the Bering Strait is opening. The main difference between the experiments from **?** and our simulations is that an opening of the Bering Strait in our simulations leads to reduced sea-ice export from the Arctic to the Atlantic, whereas their model simulates an increased export. In our simulations, the reduced ice

565 transport is also a result of a reduced sea-ice volume inside the Arctic. These differences are likely related to **?** not considering the effect of freshwater release by melting ice sheets.

A similar sign shift of the Arctic freshwater budget and transition into a slightly weaker AMOC state is also evident in simulations with prescribed ice sheets (**?**) from the ICE-6G (**?**) and GLAC-1D reconstructions (**?**) starting at about 16.09 ka and 15.86 ka, respectively (see also Table 2). The transition from a state where sea-ice export to the Atlantic is larger than

570 the freshwater input into the Arctic, to a state where the freshwater input dominates is accompanied by the development of a halocline in the Arctic ocean in the simulations with ICE-6G and GLAC-1D reconstructions (see ICE6G_P3 and GLAC1D_P3 in Table 2). However, the AMOC response in these simulations is much weaker than in the fully coupled simulations (not shown). This is likely related to a relatively low prescribed meltwater input into the Arctic, which was derived from the ice-sheet reconstructions during this time. Only around the time of MWP1A the freshwater input significantly increases. In

575 general, the simulations with coupled ice sheets show an earlier and more gradual increase in freshwater during the peak of the deglaciation, while the freshwater input into the ocean in the simulations with prescribed ice sheets is dominated by pulses of meltwater. This likely explains the different response.

Changes in river routing

The deglacial North Atlantic cooling event that is associated with enhanced river discharge into the Arctic due to changes in

580 the river routing also occurs in all our ensemble members (see Table 2). It is, consistent with D2.1, in all simulations associated with an expansion of the drainage basin of the Mackenzie River and accompanied by an AMOC slowdown. It agrees with simulations by **?**, where ice-sheets from the ICE-6G reconstructions were prescribed, as well as studies by **?** and **?**, who indicate that a rerouting of rivers caused the Younger Dryas cooling. Using a high resolution ocean–sea ice model, **?** show that freshwater discharged from the Mackenzie river is transported through the narrow coastal boundary currents towards the deep-

585 water formation sites in the Greenland and Labrador Seas, where it disrupts the open-ocean convection and thereby weakens the AMOC. In our simulations, the expansion of the Mackenzie drainage basin, due to a small retreat on the southern edge of the Laurentide ice sheet, leads to an abrupt increase in the freshwater input into the Arctic and, thereby, triggers the simulated AMOC slowdown and accompanying Northern Hemispheric cooling consistent with D2.1. In all simulations the collapse of the Laurentide ice sheet and the opening of the Hudson Bay, which allow for a rerouting of the meltwater previously entering

590 the Arctic ocean to the Hudson Bay (Fig. 13), leads to a recovery of the AMOC. The freshwater reaching the Labrador Sea through Hudson Strait flows southeastward in a coastal current and has therefore a relatively small effect on the deep convection

in the Labrador Sea. Interestingly, the timing of the change in the river routing occurs in some ensemble members before the opening of the Bering Strait (D1.1, D1.2, D1.3, D1.4), hence, in a state where the salinity in the Arctic is already reduced and the stratification is relatively stable. Despite this, all simulations show a distinct AMOC weakening in response to the enhanced Arctic freshwater input, indicating that the process itself is consistent throughout all ensemble members (not shown). The results emphasize that changes in the river routing played a crucial role in initiating the North Atlantic cooling events that occur in our simulations between about 12 ka and 9 ka (Fig. 8). Further, the AMOC recovery that follows the opening of the Hudson Bay indicates the importance of changes in the land–sea mask in response to the ice-sheet collapse and associated deglacial sea-level rise for the occurrence of abrupt events. As the changes in river routing and the opening of the Hudson Strait are in all simulations related to the gradual retreat of the Laurentide ice sheet, they appear to be deterministic and, hence, seem to be an integral part of the deglaciation.

5   Summary and Conclusion

We have applied the newly developed coupled atmosphere–ocean–vegetation–ice sheet–solid earth model MPI-ESM/mPISM/VILMA to the last deglaciation. Topography and river-routing directions are calculated according to the simulated states of ice sheets and solid Earth. By prescribing time varying atmospheric greenhouse gas concentrations, earth orbital parameters and - in most runs - a volcanic forcing as the only time dependent forcings, the coupled model is able to simulate a realistic deglaciation including abrupt millennial-scale climate events. Through an ensemble of eight simulations, we show that the simulated climate change between the LGM and PI and the simulated deglaciation is sensitive to the prescribed model parameters, particularly to the vertical background mixing in the ocean. The simulated SST anomaly between the LGM and PI of all simulations is in line with reconstructions based on proxy data. Nearly all ensemble members show a shallower, and at most a slightly weaker, NADW cell during the LGM than during PI. Interestingly, estimating the shallowing of the NADW cell from changes in the distribution of a proxy-like water mass tracer (artificial dye tracer) indicates a stronger signal than the values derived directly from the simulated AMOC. This demonstrates an additional methodological challenge in estimating past AMOC changes from sediment proxy records.

All ensemble members show abrupt cooling events. For glacial periods and during the early deglaciation, these events are caused by surges from the Laurentide and Fennoscandian ice sheets that result in the release of large amounts of icebergs into the North Atlantic, the Nordic Seas and the Arctic. The resulting meltwater input into the ocean leads to reduced surface salinity, suppressed formation of deep water and a weakened AMOC. After the end of each surge event, the system recovers to its previous state. This HE-like variability represents a glacial mode of internal climate variability of the coupled model system. However, the timing of the simulated HE-like surge events shows a considerable scatter in the model ensemble. Additional sensitivity experiments confirm, that these events are not entirely determined by the prescribed external forcing but that the initial conditions - especially of the northern hemispheric ice sheets - as well as the model parameters play an important role for the timing of these events. Except for the relatively short AMOC weakenings, the simulated AMOC in our model is always

in a strong mode, indicating a mono-stable AMOC. Performing similar experiments using a model system which simulates a weak AMOC mode for glacial climates like e.g., **?** might yield a rather different time evolution of the AMOC.

The glacial climate of the Arctic in our model system is characterized by sea-ice export to the Atlantic that exceeds the amount of freshwater input to the Arctic through river runoff, iceberg melting and precipitation minus evaporation. This effectively prevents the development of a stable halocline and causes the formation of water masses that are colder, saltier and denser than the inflowing water of North Atlantic origin. During the deglaciation, the enhanced meltwater input due to melting ice sheets together with precipitation and river runoff exceeds the amount of freshwater that is leaving the Arctic through sea-ice export. The transition towards a positive net freshwater balance leads in all simulations to the formation of an Arctic halocline. This results in the suppression of dense water formation within the Arctic and a weakening of the AMOC that is accompanied by a cooling in the North Atlantic realm. While the halocline emerges relatively abrupt in most simulations, it depends on the overall state of the Arctic Ocean, which in turn is controlled by the im- and export of waters from the adjacent seas through the major straits (specifically the Bering Strait). As the timing of the opening of those passages differs between simulations, the magnitude and abruptness of the AMOC response differ as well.

Additionally, river rerouting in connection with the opening of the Hudson Bay can cause abrupt changes in AMOC and North Atlantic climate. These processes become particularly relevant when the size of the Laurentide ice sheet is already strongly reduced. The chronological order of the opening of the Bering Strait and the river rerouting thereby substantially affects how abrupt the onset and/or offset of the events occur.

In a comprehensive comparison of the glacial and deglacial climate with proxy data, we show that the overall climate trajectory of our ensemble agrees well with observations. The validation of abrupt events in the model with proxy records is not straightforward, especially with respect to the timing of the abrupt events. Although it has been shown that HE-like surge events have a characteristic return period and are to some degree phase locked to the climate changes (**?**), the timing of the abrupt cooling events that are associated with ice-sheet surges in our ensemble are non-deterministic and largely depend on the initial conditions and model parameters. The abrupt events associated with an opening of passages or river rerouting are in principle reproducible as they occur in all ensemble members. However, the nonlinearities involved, such as ice-sheet shape, retreat as glacial isostatic adjustment make the simulation of the exact timing of these events sensitive to model parameters. Consequently, a temporal matching of the simulated abrupt events with the events derived from proxy data is difficult to achieve. In addition, the dating of proxy records is subject to a high degree of uncertainty. In conclusion, the millennial-scale climate variability in models may not align with time scales found in proxy data, so a validation should rather be based on statistical methods, similar to the model simulations of historical climate with El Niño/Southern Oscillation (e.g. **?**), rather than on the individual timing and strength of deglacial key events.

Our novel model framework presented here is a step towards a better understanding of the processes and interactions between different climate components on deglacial time scales. By including for the first time interactive Earth system components, such as ice sheets, icebergs, solid earth, and time-evolving river directions and land–sea mask into a comprehensive ESM, we reveal previously unrecognized chains of processes that explain the climate features observed throughout the last deglaciation. While in this paper we mainly focus on the overall deglacial climate response to changes in the external forcing, such as

insolation, greenhouse gases and volcanoes, as well as on the abrupt climate events that occur due to the internal variability

660 of the climate system, our ensemble will enable the analysis of a wide variety of processes in each of the individual modeled

climate components and between them. Furthermore, it emphasizes the importance of incorporating Earth system components

that are traditionally regarded as exhibiting a too-slow rate of change to be relevant for transient climate simulations.

Code and data availability. All model simulations are available on the World Data Center for Climate (WDCC): D1.1 (https://www.wdc-climate.

de/ui/entry?acronym=PMMXMC1TDIr1111), D1.2 (https://www.wdc-climate.de/ui/entry?acronym=PMMXMC1TDIr1121), D1.3 (https://

665 www.wdc-climate.de/ui/entry?acronym=PMMXMC1TDIr1131), D1.4 (https://www.wdc-climate.de/ui/entry?acronym=PMMXMC1TDIr1112),

D2.1 (https://www.wdc-climate.de/ui/entry?acronym=PMMXMC1TDIr1142), D2.2 (https://www.wdc-climate.de/ui/entry?acronym=PMMXMC1TDIr11

D2.3 (https://www.wdc-climate.de/ui/entry?acronym=PMMXMC1TDIr1162), D2.4 (https://www.wdc-climate.de/ui/entry?acronym=PMMXMC1TDIr11

NOTE LINKS WILL BE REPLACED WITH DOIS. Model data and scripts used for the analysis are available under https://doi.org/10.17617/

3.MULBNQ. Max Planck Institute Earth System Model model code is available upon request from the corresponding author. The PISM code

670 for version 0.7.3 is publicly available at Zenodo under https://doi.org/10.5281/zenodo.7541412. The VILMA source code is available upon

request from V. Klemann.

Appendix A

A1   Model parameters

A2   PalMod reconstructions

The PalMod reconstructions rely on a synthesis of marine proxy records for temperature of the last glacial cycle, the PalMod 130k marine palaeoclimate data synthesis, beta version 2.0.0 (**?**). The database includes globally distributed sea surface temperature proxies based on alkenone, TEX86, long chain diol index, Mg/Ca ratios in planktonic foraminifera, and microfossil assemblages. The global mean near-surface air temperature is computed based on the selection of records and the algorithm described in **?**. More specifically, the algorithm is an adaptation of the one used in **?** to leverage the potential of the SST record data set fully. At its core, the algorithm aggregates SST records over latitudinal bands to estimate a 60° S-60° N SST anomaly timeseries. A scaling factor of 1.9, based on an ensemble of LGM simulations (**?**), is then applied to derive the global mean temperature. The latitudinal bands and North Atlantic averages are computed by aggregating the records over the specific domain without applying a scaling factor.

A3   Modelled surface temperature bias for PI

The model shows systematic temperature biases for PI when compared to data from the ERA20C (**?**) reanalysis (Fig. A1). This near-surface air temperature bias appears in all experiments. The climate over Northeast North America is too warm, over Scandinavia and eastern Asia too cold. North Atlantic SSTs are too cold (except for the high mixing simulation D1.2). The warm bias around Antarctica is associated with an underestimation of the sea ice extent. Reduced vertical mixing reduces the bias (D1.3), enhanced mixing amplifies the bias (D1.2).

A4   Effect of vertical mixing on AMOC

A5   Temporal evolution of dye fraction on the lower boundary of NADW cell

Sedimentary proxy data have a long tradition to be used to estimate changes in the AMOC strength and geometry (e.g. **???**). In addition to methodological uncertainties intrinsic to sediment proxy data (e.g. biologically induced errors in the recording and preservation of the targeted signal, temporal changes in source functions or measurement errors), the interpretation of the determined variations in terms of changes in AMOC geometry or strength is not straightforward. The dye fraction provides some insights into the temporal evolution of the signal within a consistent model system including a well-defined constant source function at the surface (1 for the northern Atlantic and Arctic surface waters and 0 for the remaining ocean surface, including the Southern Ocean deep water source regions).

Figure A4 supplements the information given in Figure 10 and displays the temporal evolution of the zonally averaged dye fraction on the water mass boundary between NADW and southern source deep waters, defined by AMOC=0, for the latitudinal range from 30° S to 40° N over the entire deglaciation. Overall, the dye fraction increases by 0.1 to 0.15 from the LGM to
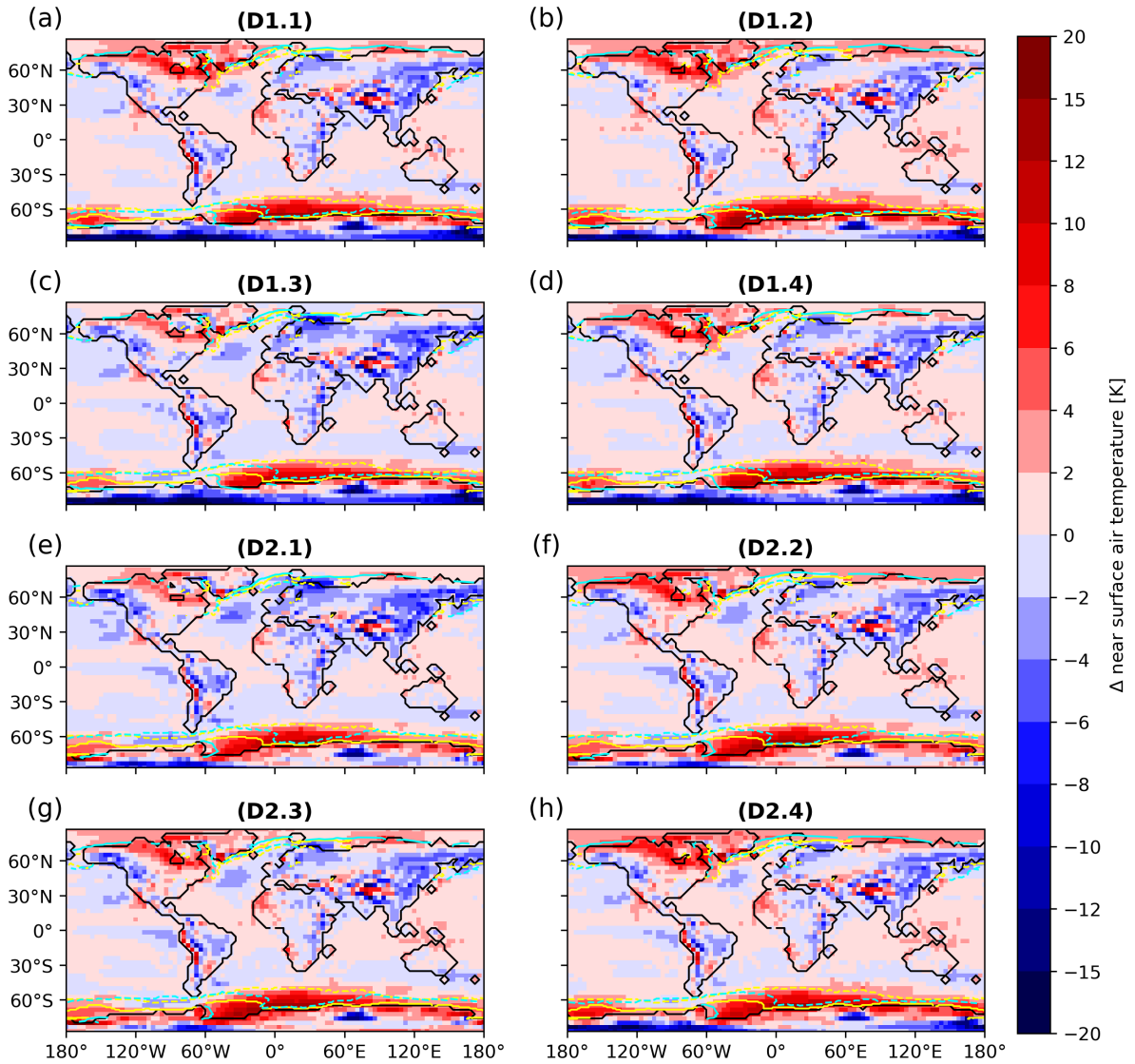
Figure A1. Difference in annual mean near-surface air temperature between model and ERA-20C (**?**) reanalysis (colours, averaged over 1901 to 1955). Panels (a-h) show individual ensemble members. The isolines show the sea-ice extent (> 0.15 sea-ice coverage in the long-term mean seasonal climatology) from years 1900 to 1955 of the HadiSST dataset (**?**) for summer (yellow solid) and winter (yellow dashed) and from the model for summer (cyan solid) and winter (cyan dashed). The land–sea mask is indicated by the solid black lines.
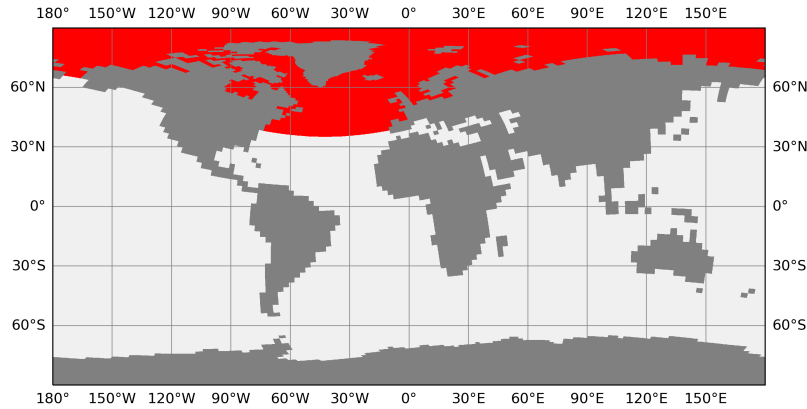
Figure A2. Source function for the NADW dye tracer with 1 (red) in the northern Atlantic and the Arctic and 0 (light grey) at the remaining ocean surface.
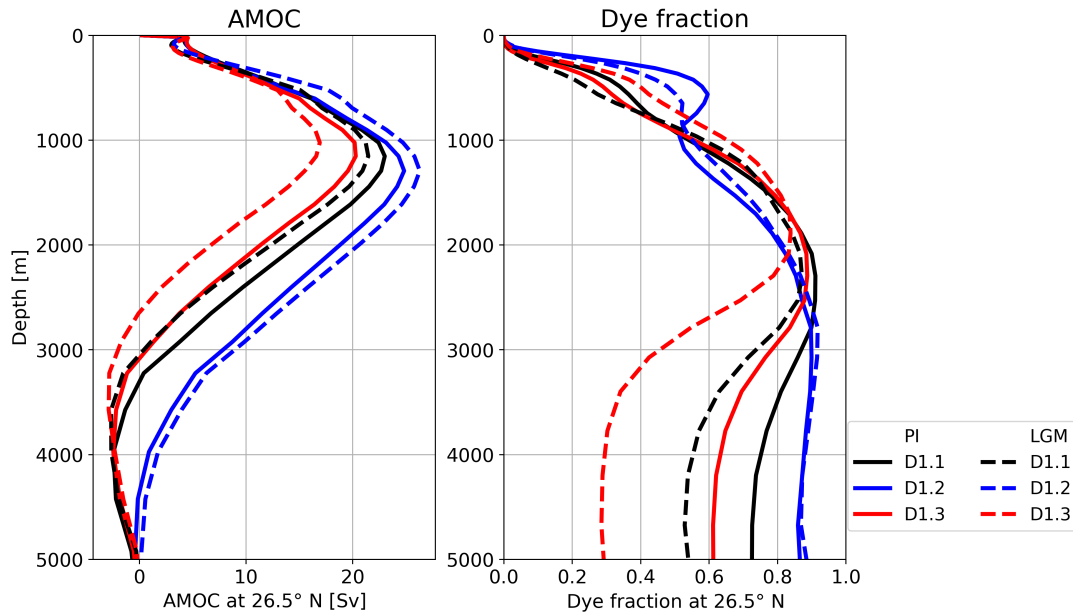
Figure A3. As Figs. 4a and 4c, but for selected ensemble members with different vertical background mixing rates: D1.3 has the lowest rate, D1.2 the highest (see Table A1). Solid lines represent the PI state and dashed lines the LGM state. The data show an average over the periods from 23 to 18 ka and from 1.1 to 0.1 ka. The simulations have been started from the same spin-up state at 26 ka.

present day at all latitudes with a larger increase in the southern hemisphere when the NADW reaches further south during PI (Fig. 5). It can be assumed that a similar temporal shift occurs in proxy data, which are used to estimates the AMOC geometry. The interpretation of these proxy data might, in turn, lead to a biased AMOC geometry or to the assumption that the source function of the proxy must have changed over time.
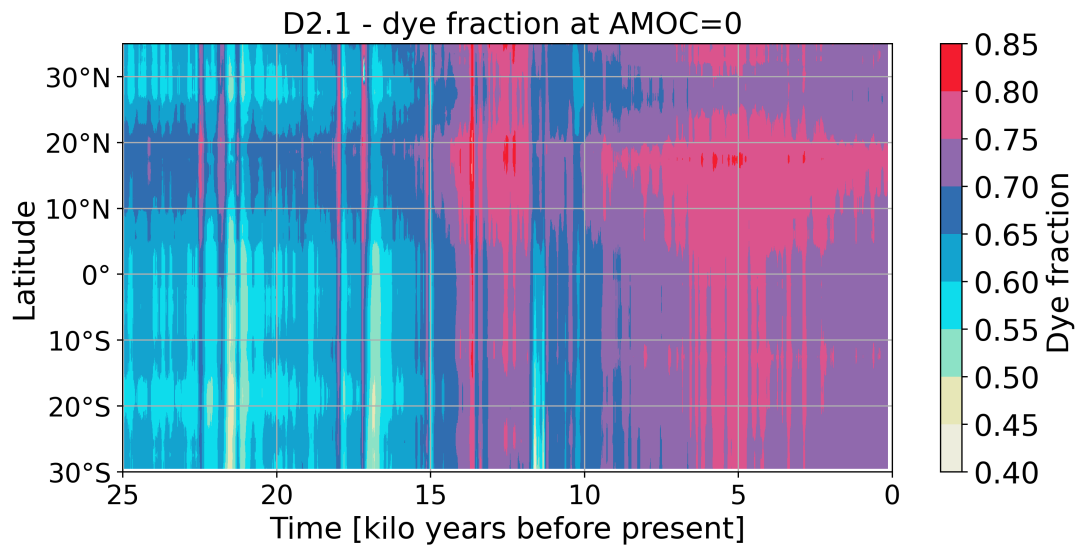
Figure A4. Time evolution of the zonal mean dye fraction at the depth of AMOC=0 for latitudes between 30° S and 40° N in simulation D2.1. Data shown are 100-year running means.

Additionally, we find that the latitudinal pattern in the dye fraction does not evolve uniformly over time. In particular, larger variations in the dye fraction are present in the southern hemisphere than in the northern during abrupt events. The reconstruction of Atlantic water mass properties from sediment core data which are distributed over the whole Atlantic north of 30° S could be complicated by this latitudinal modulation of the dye fraction. As already stated in the main text, we do not claim that our dye fraction represents real world proxy data, but within our consistent model system we find additional sources of uncertainties which might complicate the reconstruction of the AMOC geometry based on proxy data.

A6   Ice volumes at the LGM and PI

Author contributions. UM designed the study and performed all simulations. UM, MLK, CS and KDS analyzed the data and wrote the first draft of the manuscript. UM, MLK, FAZ, CS, MB, OE, VG, VK, VLM, AM, TR, and KDS took part in the development of the coupled model. JPB generated the PalMod proxy reconstructions. All authors critically discussed the results and provided valuable feedback during the manuscript compilation.

Competing interests. The authors declare that they have no conflict of interest.

Acknowledgements. The project was funded by the German Federal Ministry of Education and Research as a Research for Sustainability Initiative through the PalMod project (grant nos. 01LP1916A, 01LP1917B, 01LP1915C, 01LP2302A, 01LP2316A, 01LP2318A, 01LP1918A and 01L2305A). This work also received funding from the European Union's Horizon 2020 research and innovation program (Marie Sklodowska-Curie grant agreement No 660893). All model simulations were performed at the German Climate Computing Center. Enrico Degregori optimized the performance of the model code. Matthew Toohey supplied the annually varying volcanic forcing. Thomas Kleinen supported the optimization of the algorithm for the adaptation of the land–sea mask. The authors thank Johann Jungclaus, Louise Sime and Sam Sherriff-Tadano for critical feedback and valuable suggestions which helped to improve the manuscript.

References

Albrecht, T., Winkelmann, R., and Levermann, A.: Glacial-cycle simulations of the Antarctic Ice Sheet with the Parallel Ice Sheet Model (PISM) – Part 2: Parameter ensemble analysis, The Cryosphere, 14, 633–656, https://doi.org/10.5194/tc-14-633-2020, 2020.

Albrecht, T., Bagge, M., and Klemann, V.: Feedback mechanisms controlling Antarctic glacial-cycle dynamics simulated with a coupled ice sheet–solid Earth model, The Cryosphere, 18, 4233–4255, https://doi.org/10.5194/tc-18-4233-2024, 2024.

Annan, J. D., Hargreaves, J. C., and Mauritsen, T.: A new global surface temperature reconstruction for the Last Glacial Maximum, Climate of the Past, 18, 1883–1896, https://doi.org/10.5194/cp-18-1883-2022, 2022.

Arakawa, A. and Lamb, V. R.: Computational Design of the Basic Dynamical Processes of the UCLA General Circulation Model, p. 173–265, Elsevier, https://doi.org/10.1016/b978-0-12-460817-7.50009-4, 1977.

Bard, E., Hamelin, B., and Delanghe-Sabatier, D.: Deglacial Meltwater Pulse 1B and Younger Dryas Sea Levels Revisited with Boreholes at Tahiti, Science, 327, 1235–1237, https://doi.org/10.1126/science.1180557, 2010.

Baudouin, J.-P., Weitzel, N., May, M., Jonkers, L., Dolman, A. M., and Rehfeld, K.: Testing the reliability of global surface temperature reconstructions of the last glacial cycle, https://doi.org/10.5194/egusphere-2024-1387, 2024.

Bereiter, B., Shackleton, S., Baggenstos, D., Kawamura, K., and Severinghaus, J.: Mean global ocean temperatures during the last glacial transition, Nature, 553, 39–44, https://doi.org/10.1038/nature25152, 2018.

Berger, A. and Loutre, M.: Insolation values for the climate of the last 10 million years, Quaternary Science Reviews, 10, 297 – 317, https://doi.org/https://doi.org/10.1016/0277-3791(91)90033-Q, 1991.

Bouttes, N., Lhardy, F., Quiquet, A., Paillard, D., Goosse, H., and Roche, D. M.: Deglacial climate changes as forced by different ice sheet reconstructions, Climate of the Past, 19, 1027–1042, https://doi.org/10.5194/cp-19-1027-2023, 2023.

Briggs, R. D., Pollard, D., and Tarasov, L.: A data-constrained large ensemble analysis of Antarctic evolution since the Eemian, Quaternary Science Reviews, 103, 91 – 115, https://doi.org/https://doi.org/10.1016/j.quascirev.2014.09.003, 2014.

Buizert, C., Gkinis, V., Severinghaus, J. P., He, F., Lecavalier, B. S., Kindler, P., Leuenberger, M., Carlson, A. E., Vinther, B., Masson-Delmotte, V., White, J. W. C., Liu, Z., Otto-Bliesner, B., and Brook, E. J.: Greenland temperature response to climate forcing during the last deglaciation, Science, 345, 1177–1180, https://doi.org/10.1126/science.1254961, 2014.

Carlson, A. E., Clark, P. U., Haley, B. A., Klinkhammer, G. P., Simmons, K., Brook, E. J., and Meissner, K. J.: Geochemical proxies of North American freshwater routing during the Younger Dryas cold event, Proceedings of the National Academy of Sciences, 104, 6556–6561, https://doi.org/10.1073/pnas.0611313104, 2007.

Charbit, S., Kageyama, M., Roche, D., Ritz, C., and Ramstein, G.: Investigating the mechanisms leading to the deglaciation of past continental northern hemisphere ice sheets with the CLIMBER–GREMLINS coupled model, Global and Planetary Change, 48, 253–273, https://doi.org/10.1016/j.gloplacha.2005.01.002, 2005.

Clark, P. U., Pisias, N. G., Stocker, T. F., and Weaver, A. J.: The role of the thermohaline circulation in abrupt climate change, Nature, 415, 863–869, https://doi.org/10.1038/415863a, 2002.

Condron, A. and Winsor, P.: Meltwater routing and the Younger Dryas, Proceedings of the National Academy of Sciences, 109, 19 928–19 933, https://doi.org/10.1073/pnas.1207381109, 2012.

Deschamps, P., Durand, N., Bard, E., Hamelin, B., Camoin, G., Thomas, A. L., Henderson, G. M., Okuno, J., and Yokoyama, Y.: Ice-sheet collapse and sea-level rise at the Bølling warming 14, 600 years ago, Nature, 483, 559–564, https://doi.org/10.1038/nature10902, 2012.

Dolman, A. M. and Laepple, T.: Sedproxy: a forward model for sediment-archived climate proxies, Climate of the Past, 14, 1851–1868, https://doi.org/10.5194/cp-14-1851-2018, 2018.

Duplessy, J. C., Shackleton, N. J., Fairbanks, R. G., Labeyrie, L., Oppo, D., and Kallel, N.: Deepwater source varia-tions during the last climatic cycle and their impact on the global deepwater circulation, Paleoceanography, 3, 343–360, https://doi.org/10.1029/pa003i003p00343, 1988.

Dyke, A. S. and Savelle, J. M.: Holocene History of the Bering Sea Bowhead Whale (Balaena mysticetus) in Its Beau-fort Sea Summer Grounds off Southwestern Victoria Island, Western Canadian Arctic, Quaternary Research, 55, 371–379, https://doi.org/https://doi.org/10.1006/qres.2001.2228, 2001.

Elias, S. A., Short, S. K., Nelson, C. H., and Birks, H. H.: Life and times of the Bering land bridge, Nature, 382, 60–63, https://doi.org/10.1038/382060a0, 1996.

England, J.: Coalescent Greenland and Innuitian ice during the Last Glacial Maximum: revising the Quaternary of the Canadian High Arctic, Quaternary Science Reviews, 18, 421–456, https://doi.org/10.1016/s0277-3791(98)00070-5, 1999.

England, J., Atkinson, N., Bednarski, J., Dyke, A., Hodgson, D., and Ó Cofaigh, C.: The Innuitian Ice Sheet: configuration, dynamics and chronology, Quaternary Science Reviews, 25, 689–703, https://doi.org/10.1016/j.quascirev.2005.08.007, 2006.

England, J. H. and Furze, M. F.: New evidence from the western Canadian Arctic Archipelago for the resubmergence of Bering Strait, Quaternary Research, 70, 60–67, https://doi.org/10.1016/j.yqres.2008.03.001, 2008.

Erokhina, O. and Mikolajewicz, U.: A New Eulerian Iceberg Module for Climate Studies, Journal of Advances in Modeling Earth Systems, 16, https://doi.org/10.1029/2023ms003807, 2024.

Fairbanks, R. G.: A 17, 000-year glacio-eustatic sea level record: influence of glacial melting rates on the Younger Dryas event and deep-ocean circulation, Nature, 342, 637–642, https://doi.org/10.1038/342637a0, 1989.

Frajka-Williams, E., Ansorge, I. J., Baehr, J., Bryden, H. L., Chidichimo, M. P., Cunningham, S. A., Danabasoglu, G., Dong, S., Donohue, K. A., Elipot, S., Heimbach, P., Holliday, N. P., Hummels, R., Jackson, L. C., Karstensen, J., Lankhorst, M., Le Bras, I. A., Lozier, M. S., McDonagh, E. L., Meinen, C. S., Mercier, H., Moat, B. I., Perez, R. C., Piecuch, C. G., Rhein, M., Srokosz, M. A., Trenberth, K. E., Bacon, S., Forget, G., Goni, G., Kieke, D., Koelling, J., Lamont, T., McCarthy, G. D., Mertens, C., Send, U., Smeed, D. A., Speich, S., van den Berg, M., Volkov, D., and Wilson, C.: Atlantic Meridional Overturning Circulation: Observed Transport and Variability, Frontiers in Marine Science, 6, https://doi.org/10.3389/fmars.2019.00260, 2019.

Friedrich, T., Timmermann, A., Tigchelaar, M., Elison Timm, O., and Ganopolski, A.: Nonlinear climate sensitivity and its implications for future greenhouse warming, Science Advances, 2, https://doi.org/10.1126/sciadv.1501923, 2016.

Ganopolski, A. and Brovkin, V.: Simulation of climate, ice sheets and COamp;lt;subamp;gt;2amp;lt;/subamp;gt; evolution during the last four glacial cycles with an Earth system model of intermediate complexity, Climate of the Past, 13, 1695–1716, https://doi.org/10.5194/cp-13-1695-2017, 2017.

Gowan, E. J., Zhang, X., Khosravi, S., Rovere, A., Stocchi, P., Hughes, A. L. C., Gyllencreutz, R., Mangerud, J., Svend-sen, J.-I., and Lohmann, G.: A new global ice sheet reconstruction for the past 80 000 years, Nature Communications, 12, https://doi.org/10.1038/s41467-021-21469-w, 2021.

Gu, S., Liu, Z., Oppo, D. W., Lynch-Stieglitz, J., Jahn, A., Zhang, J., and Wu, L.: Assessing the potential capability of reconstruct-ing glacial Atlantic water masses and AMOC using multiple proxies in CESM, Earth and Planetary Science Letters, 541, 116 294, https://doi.org/10.1016/j.epsl.2020.116294, 2020.

Hagemann, S. and Dümenil, L.: Documentation for the Hydrological Discharge Model, Tech. rep., Max Planck Institute for Meteorology, 1998.

800 Harrison, S. P., Bartlein, P. J., Izumi, K., Li, G., Annan, J., Hargreaves, J., Braconnot, P., and Kageyama, M.: Evaluation of CMIP5 palaeo-simulations to improve climate projections, Nature Climate Change, 5, 735–743, https://doi.org/10.1038/nclimate2649, 2015.

He, C., Liu, Z., Otto-Bliesner, B. L., Brady, E., Zhu, C., Tomas, R., Clark, P., Zhu, J., Jahn, A., Gu, S., Zhang, J., Nusbaumer, J., Noone, D., Cheng, H., Wang, Y., Yan, M., and Bao, Y.: Hydroclimate footprint of pan-Asian monsoon water isotope during the last deglaciation, Science Advances, 7, https://doi.org/10.1126/sciadv.abe2611, 2021.

805 Heinemann, M., Timmermann, A., Elison Timm, O., Saito, F., and Abe-Ouchi, A.: Deglacial ice sheet meltdown: orbital pacemaking and CO<subamp;gt;2amp;lt;/subamp;gt; effects, Climate of the Past, 10, 1567–1579, https://doi.org/10.5194/cp-10-1567-2014, 2014.

Heinrich, H.: Origin and consequences of cyclic ice rafting in the Northeast Atlantic Ocean during the past 130,000 years, Quaternary Research, 29, 142–152, https://doi.org/https://doi.org/10.1016/0033-5894(88)90057-9, 1988.

Hemming, S. R.: Heinrich events: Massive late Pleistocene detritus layers of the North Atlantic and their global climate imprint, Reviews of 810 Geophysics, 42, https://doi.org/10.1029/2003rg000128, 2004.

Hibler, W. D.: A Dynamic Thermodynamic Sea Ice Model, Journal of Physical Oceanography, 9, 815–846, https://doi.org/10.1175/1520-0485(1979)009<0815:adtsim>2.0.co;2, 1979.

Howe, J. N. W., Piotrowski, A. M., Noble, T. L., Mulitza, S., Chiessi, C. M., and Bayon, G.: North Atlantic Deep Water Production during the Last Glacial Maximum, Nature Communications, 7, https://doi.org/10.1038/ncomms11765, 2016.

815 Hu, A., Otto-Bliesner, B. L., Meehl, G. A., Han, W., Morrill, C., Brady, E. C., and Briegleb, B.: Response of Thermo-haline Circulation to Freshwater Forcing under Present-Day and LGM Conditions, Journal of Climate, 21, 2239 – 2258, https://doi.org/10.1175/2007JCLI1985.1, 2008.

Hu, A., Meehl, G. A., Han, W., Timmermann, A., Otto-Bliesner, B., Liu, Z., Washington, W. M., Large, W., Abe-Ouchi, A., Kimoto, M., Lambeck, K., and Wu, B.: Role of the Bering Strait on the hysteresis of the ocean conveyor belt circulation and glacial climate stability, 820 Proceedings of the National Academy of Sciences, 109, 6417–6422, https://doi.org/10.1073/pnas.1116014109, 2012.

Hu, A., Meehl, G. A., Han, W., Otto-Bliestner, B., Abe-Ouchi, A., and Rosenbloom, N.: Effects of the Bering Strait closure on AMOC and global climate under different background climates, Progress in Oceanography, 132, 174–196, https://doi.org/10.1016/j.pocean.2014.02.004, 2015.

Hughes, A. L. C., Gyllencreutz, R., Lohne, S., Mangerud, J., and Svendsen, J. I.: The last Eurasian ice sheets – a chronological database and 825 time-slice reconstruction, DATED-1, Boreas, 45, 1–45, https://doi.org/10.1111/bor.12142, 2015.

Hunke, E. C. and Dukowicz, J. K.: An Elastic–Viscous–Plastic Model for Sea Ice Dynamics, Journal of Physical Oceanography, 27, 1849–1867, https://doi.org/10.1175/1520-0485(1997)027<1849:aevpmf>2.0.co;2, 1997.

Hurrell, J. W., Hack, J. J., Shea, D., Caron, J. M., and Rosinski, J.: A New Sea Surface Temperature and Sea Ice Boundary Dataset for the Community Atmosphere Model, Journal of Climate, 21, 5145–5153, https://doi.org/10.1175/2008jcli2292.1, 2008.

830 Ivanovic, R. F., Gregoire, L. J., Kageyama, M., Roche, D. M., Valdes, P. J., Burke, A., Drummond, R., Peltier, W. R., and Tarasov, L.: Transient climate simulations of the deglaciation 21–9 thousand years before present (version 1) – PMIP4 Core experiment design and boundary conditions, Geoscientific Model Development, 9, 2563–2587, https://doi.org/10.5194/gmd-9-2563-2016, 2016.

Jakobsson, M., Pearce, C., Cronin, T. M., Backman, J., Anderson, L. G., Barrientos, N., Björk, G., Coxall, H., de Boer, A., Mayer, L. A., Mörth, C.-M., Nilsson, J., Rattray, J. E., Stranne, C., Semiletov, I., and O'Regan, M.: Post-glacial flooding of the Bering Land Bridge dated

835   to 11calkaBP based on new geophysical and sediment records, Climate of the Past, 13, 991–1005, https://doi.org/10.5194/cp-13-991-2017, 2017.

Jonkers, L., Cartapanis, O., Langner, M., McKay, N., Mulitza, S., Strack, A., and Kucera, M.: Integrating palaeoclimate time series with rich metadata for uncertainty modelling: strategy and documentation of the PalMod 130k marine palaeoclimate data synthesis, Earth System Science Data, 12, 1053–1081, https://doi.org/10.5194/essd-12-1053-2020, 2020.

840   Jungclaus, J. H., Fischer, N., Haak, H., Lohmann, K., Marotzke, J., Matei, D., Mikolajewicz, U., Notz, D., and von Storch, J. S.: Characteristics of the ocean simulations in the Max Planck Institute Ocean Model (MPIOM) the ocean component of the MPI-Earth system model, Journal of Advances in Modeling Earth Systems, 5, 422–446, https://doi.org/10.1002/jame.20023, 2013.

Kageyama, M., Harrison, S. P., Kapsch, M.-L., Löfverström, M., Lora, J. M., Mikolajewicz, U., Sherriff-Tadano, S., Vadsaria, T., Abe-Ouchi, A., Bouttes, N., Chandan, D., LeGrande, A. N., Lhardy, F., Lohmann, G., Morozova, P. A., Ohgaito, R., Peltier, W. R., Quiquet, A., Roche,
845   D. M., Shi, X., Schmittner, A., Tierney, J. E., and Volodin, E.: The PMIP4-CMIP6 Last Glacial Maximum experiments: preliminary results and comparison with the PMIP3-CMIP5 simulations, Climate of the Past Discussions, 2020, 1–37, https://doi.org/10.5194/cp-2019-169, 2020.

Kageyama, M., Harrison, S. P., Kapsch, M.-L., Lofverstrom, M., Lora, J. M., Mikolajewicz, U., Sherriff-Tadano, S., Vadsaria, T., Abe-Ouchi, A., Bouttes, N., Chandan, D., Gregoire, L. J., Ivanovic, R. F., Izumi, K., LeGrande, A. N., Lhardy, F., Lohmann, G., Morozova, P. A.,
850   Ohgaito, R., Paul, A., Peltier, W. R., Poulsen, C. J., Quiquet, A., Roche, D. M., Shi, X., Tierney, J. E., Valdes, P. J., Volodin, E., and Zhu, J.: The PMIP4 Last Glacial Maximum experiments: preliminary results and comparison with the PMIP3 simulations, Climate of the Past, 17, 1065–1089, https://doi.org/10.5194/cp-17-1065-2021, 2021.

Kapsch, M.-L., Mikolajewicz, U., Ziemen, F. A., Rodehacke, C. B., and Schannwell, C.: Analysis of the surface mass balance for deglacial climate simulations, The Cryosphere, 15, 1131–1156, https://doi.org/10.5194/tc-15-1131-2021, 2021.

855   Kapsch, M.-L., Mikolajewicz, U., Ziemen, F., and Schannwell, C.: Ocean Response in Transient Simulations of the Last Deglaciation Dominated by Underlying Ice-Sheet Reconstruction and Method of Meltwater Distribution, Geophysical Research Letters, 49, e2021GL096 767, https://doi.org/https://doi.org/10.1029/2021GL096767, 2022.

Karami, M. P., Myers, P. G., de Vernal, A., Tremblay, L. B., and Hu, X.: The role of Arctic gateways on sea ice and circulation in the Arctic and North Atlantic Oceans: a sensitivity study with an ocean-sea-ice model, Climate Dynamics, 57, 2129–2151,
860   https://doi.org/10.1007/s00382-021-05798-6, 2021.

Kaufman, D. S. and Broadman, E.: Revisiting the Holocene global temperature conundrum, Nature, 614, 425–435, https://doi.org/10.1038/s41586-022-05536-w, 2023.

Keigwin, L. D., Donnelly, J. P., Cook, M. S., Driscoll, N. W., and Brigham-Grette, J.: Rapid sea-level rise and Holocene climate in the Chukchi Sea, Geology, 34, 861, https://doi.org/10.1130/g22712.1, 2006.

865   Köhler, P., Nehrbass-Ahles, C., Schmitt, J., Stocker, T. F., and Fischer, H.: A 156 kyr smoothed history of the atmospheric greenhouse gases CO_2, CH_4, and N_2O and their radiative forcing, Earth System Science Data, 9, 363–387, https://doi.org/10.5194/essd-9-363-2017, 2017.

Konrad, H., Sasgen, I., Pollard, D., and Klemann, V.: Potential of the solid-Earth response for limiting long-term West Antarctic Ice Sheet retreat in a warming climate, Earth and Planetary Science Letters, 432, 254–264, https://doi.org/10.1016/j.epsl.2015.10.008, 2015.

Lambeck, K., Rouby, H., Purcell, A., Sun, Y., and Sambridge, M.: Sea level and global ice volumes from the Last Glacial Maximum to the
870   Holocene, Proceedings of the National Academy of Sciences, 111, 15 296–15 303, https://doi.org/10.1073/pnas.1411762111, 2014.

LeGrand, P. and Wunsch, C.: Constraints from paleotracer data on the North Atlantic circulation during the Last Glacial Maximum, Paleoceanography, 10, 1011–1045, https://doi.org/10.1029/95pa01455, 1995.

Liu, Z.: Evolution of Atlantic Meridional Overturning Circulation since the last glaciation: model simulations and relevance to present and future, Philosophical Transactions of the Royal Society A: Mathematical, Physical and Engineering Sciences, 381, https://doi.org/10.1098/rsta.2022.0190, 2023.

Liu, Z., Otto-Bliesner, B. L., He, F., Brady, E. C., Tomas, R., Clark, P. U., Carlson, A. E., Lynch-Stieglitz, J., Curry, W., Brook, E., Erickson, D., Jacob, R., Kutzbach, J., and Cheng, J.: Transient Simulation of Last Deglaciation with a New Mechanism for Bølling-Allerød Warming, Science, 325, 310–314, https://doi.org/10.1126/science.1171041, 2009.

Lynch-Stieglitz, J., Schmidt, M. W., Gene Henry, L., Curry, W. B., Skinner, L. C., Mulitza, S., Zhang, R., and Chang, P.: Muted change in Atlantic overturning circulation over some glacial-aged Heinrich events, Nature Geoscience, 7, 144–150, https://doi.org/10.1038/ngeo2045, 2014.

MacAyeal, D. R.: Binge/purge oscillations of the Laurentide Ice Sheet as a cause of the North Atlantic's Heinrich events, Paleoceanography, 8, 775–784, https://doi.org/10.1029/93pa02200, 1993.

Maier-Reimer, E. and Mikolajewicz, U.: Experiments with an OGCM on the cause of the Younger Dryas, 1989.

Maris, M. N. A., de Boer, B., Ligtenberg, S. R. M., Crucifix, M., van de Berg, W. J., and Oerlemans, J.: Modelling the evolution of the Antarctic ice sheet since the last interglacial, The Cryosphere, 8, 1347–1360, https://doi.org/10.5194/tc-8-1347-2014, 2014.

Martinec, Z., Klemann, V., van der Wal, W., Riva, R. E. M., Spada, G., Sun, Y., Melini, D., Kachuck, S. B., Barletta, V., Simon, K., A, G., and James, T. S.: A benchmark study of numerical implementations of the sea level equation in GIA modelling, Geophysical Journal International, 215, 389–414, https://doi.org/10.1093/gji/ggy280, 2018.

Mauritsen, T., Bader, J., Becker, T., Behrens, J., Bittner, M., Brokopf, R., Brovkin, V., Claussen, M., Crueger, T., Esch, M., Fast, I., Fiedler, S., Fläschner, D., Gayler, V., Giorgetta, M., Goll, D. S., Haak, H., Hagemann, S., Hedemann, C., Hohenegger, C., Ilyina, T., Jahns, T., Jimenez-de-la Cuesta, D., Jungclaus, J., Kleinen, T., Kloster, S., Kracher, D., Kinne, S., Kleberg, D., Lasslop, G., Kornblueh, L., Marotzke, J., Matei, D., Meraner, K., Mikolajewicz, U., Modali, K., Möbis, B., Müller, W. A., Nabel, J. E. M. S., Nam, C. C. W., Notz, D., Nyawira, S.-S., Paulsen, H., Peters, K., Pincus, R., Pohlmann, H., Pongratz, J., Popp, M., Raddatz, T. J., Rast, S., Redler, R., Reick, C. H., Rohrschneider, T., Schemann, V., Schmidt, H., Schnur, R., Schulzweida, U., Six, K. D., Stein, L., Stemmler, I., Stevens, B., von Storch, J.-S., Tian, F., Voigt, A., Vrese, P., Wieners, K.-H., Wilkenskjeld, S., Winkler, A., and Roeckner, E.: Developments in the MPI-M Earth System Model version 1.2 (MPI-ESM1.2) and its response to increasing CO2, Journal of Advances in Modeling Earth Systems, 11, 998–1038, https://doi.org/https://doi.org/10.1029/2018MS001400, 2019.

McManus, J. F., Francois, R., Gherardi, J. M., Keigwin, L. D., and Brown-Leger, S.: Collapse and rapid resumption of Atlantic meridional circulation linked to deglacial climate changes, Nature, 428, 834–837, https://doi.org/10.1038/nature02494, 2004.

Meccia, V. L. and Mikolajewicz, U.: Interactive ocean bathymetry and coastlines for simulating the last deglaciation with the Max Planck Institute Earth System Model (MPI-ESM-v1.2), Geoscientific Model Development, 11, 4677–4692, https://doi.org/10.5194/gmd-11-4677-2018, 2018.

Menviel, L., Yu, J., Joos, F., Mouchet, A., Meissner, K. J., and England, M. H.: Poorly ventilated deep ocean at the Last Glacial Maximum inferred from carbon isotopes: A data-model comparison study, Paleoceanography, 32, 2–17, https://doi.org/10.1002/2016pa003024, 2017.

Mikolajewicz, U., Gröger, M., Maier-Reimer, E., Schurgers, G., Vizcaíno, M., and Winguth, A. M. E.: Long-term effects of anthropogenic CO2 emissions simulated with a complex earth system model, Climate Dynamics, 28, 599–633, https://doi.org/10.1007/s00382-006-0204-y, 2007a.

Mikolajewicz, U., Vizcaíno, M., Jungclaus, J., and Schurgers, G.: Effect of ice sheet interactions in anthropogenic climate change simulations, Geophysical Research Letters, 34, https://doi.org/10.1029/2007gl031173, 2007b.

Mikolajewicz, U., Ziemen, F., Cioni, G., Claussen, M., Fraedrich, K., Heidkamp, M., Hohenegger, C., Jimenez de la Cuesta, D., Kapsch, M.-L., Lemburg, A., Mauritsen, T., Meraner, K., Röber, N., Schmidt, H., Six, K. D., Stemmler, I., Tamarin-Brodsky, T., Winkler, A., Zhu, X., and Stevens, B.: The climate of a retrograde rotating Earth, Earth System Dynamics, 9, 1191–1215, https://doi.org/10.5194/esd-9-1191-2018, 2018.

915   Moat, B. I., Smeed, D., Rayner, D., Johns, W. E., Smith, R. H., Volkov, D. L., Baringer, M. O., and Collins, J.: Atlantic meridional overturning circulation observed by the RAPID-MOCHA-WBTS (RAPID-Meridional Overturning Circulation and Heatflux Array-Western Boundary Time Series) array at 26N from 2004 to 2022 (v2022.1)., https://doi.org/10.5285/04C79ECE-3186-349A-E063-6C86ABC0158C, 2023.

Muntjewerf, L., Petrini, M., Vizcaino, M., Ernani da Silva, C., Sellevold, R., Scherrenberg, M. D. W., Thayer-Calder, K., Bradley, S. L., Lenaerts, J. T. M., Lipscomb, W. H., and Lofverstrom, M.: Greenland Ice Sheet Contribution to 21st Century Sea Level Rise as Simulated

920   by the Coupled CESM2.1-CISM2.1, Geophysical Research Letters, 47, https://doi.org/10.1029/2019gl086836, 2020.

Obase, T. and Abe-Ouchi, A.: Abrupt Bølling-Allerød Warming Simulated under Gradual Forcing of the Last Deglaciation, Geophysical Research Letters, 46, 11 397–11 405, https://doi.org/10.1029/2019gl084675, 2019.

Obase, T., Menviel, L., Abe-Ouchi, A., Vadsaria, T., Ivanovic, R., Snoll, B., Sherriff-Tadano, S., Valdes, P., Gregoire, L., Kapsch, M.-L., Mikolajewicz, U., Bouttes, N., Roche, D., Lhardy, F., He, C., Otto-Bliesner, B., Liu, Z., and Chan, W.-L.: Multi-model assessment of the

925   deglacial climatic evolution at high southern latitudes, Climate of the Past Discussions, https://doi.org/10.5194/cp-2023-86, 2023.

Oppo, D. W. and Lehman, S. J.: Mid-Depth Circulation of the Subpolar North Atlantic During the Last Glacial Maximum, Science, 259, 1148–1152, https://doi.org/10.1126/science.259.5098.1148, 1993.

Oppo, D. W., Gebbie, G., Huang, K., Curry, W. B., Marchitto, T. M., and Pietro, K. R.: Data Constraints on Glacial Atlantic Water Mass Geometry and Properties, Paleoceanography and Paleoclimatology, 33, 1013–1034, https://doi.org/10.1029/2018pa003408, 2018.

930   Osman, M., Tierney, J. E., Zhu, J., and et al.: Globally resolved surface temperatures since the Last Glacial Maximum, Nature, pp. 239–244, https://doi.org/10.1038/s41586-021-03984-4, 2021.

Pacanowski, R. C. and Philander, S. G. H.: Parameterization of Vertical Mixing in Numerical Models of Tropical Oceans, Journal of Physical Oceanography, 11, 1443–1451, https://doi.org/10.1175/1520-0485(1981)011<1443:povmin>2.0.co;2, 1981.

Paul, A., Mulitza, S., Stein, R., and Werner, M.: A global climatology of the ocean surface during the Last Glacial Maximum mapped on a

935   regular grid (GLOMAP), Climate of the Past, 17, 805–824, https://doi.org/10.5194/cp-17-805-2021, 2021.

Peltier, W. R., Argus, D. F., and Drummond, R.: Space geodesy constrains ice age terminal deglaciation: The global ICE-6G_C (VM5a) model, Journal of Geophysical Research: Solid Earth, 120, 450–487, https://doi.org/10.1002/2014JB011176, 2015.

Planton, Y. Y., Guilyardi, E., Wittenberg, A. T., Lee, J., Gleckler, P. J., Bayr, T., McGregor, S., McPhaden, M. J., Power, S., Roehrig, R., Vialard, J., and Voldoire, A.: Evaluating Climate Models with the CLIVAR 2020 ENSO Metrics Package, Bulletin of the American

940   Meteorological Society, 102, E193–E217, https://doi.org/10.1175/bams-d-19-0337.1, 2021.

Poli, P., Hersbach, H., Dee, D. P., Berrisford, P., Simmons, A. J., Vitart, F., Laloyaux, P., Tan, D. G. H., Peubey, C., Thépaut, J.-N., Trémolet, Y., Hólm, E. V., Bonavita, M., Isaksen, L., and Fisher, M.: ERA-20C: An Atmospheric Reanalysis of the Twentieth Century, Journal of Climate, 29, 4083–4097, https://doi.org/10.1175/jcli-d-15-0556.1, 2016.

Pollard, D., Gomez, N., and Deconto, R. M.: Variations of the Antarctic Ice Sheet in a Coupled Ice Sheet-Earth-Sea Level Model: Sensitivity

945   to Viscoelastic Earth Properties, Journal of Geophysical Research: Earth Surface, 122, 2124–2138, https://doi.org/10.1002/2017jf004371, 2017.

Pöppelmeier, F., Jeltsch-Thömmes, A., Lippold, J., Joos, F., and Stocker, T. F.: Multi-proxy constraints on Atlantic circulation dynamics since the last ice age, Nature Geoscience, 16, 349–356, https://doi.org/10.1038/s41561-023-01140-3, 2023.

Quiquet, A., Roche, D. M., Dumas, C., Bouttes, N., and Lhardy, F.: Climate and ice sheet evolutions from the last glacial maximum to the pre-industrial period with an ice-sheet–climate coupled model, Climate of the Past, 17, 2179–2199, https://doi.org/10.5194/cp-17-2179-2021, 2021.

Reick, C. H., Raddatz, T., Brovkin, V., and Gayler, V.: Representation of natural and anthropogenic land cover change in MPI-ESM, Journal of Advances in Modeling Earth Systems, 5, 459–482, https://doi.org/10.1002/jame.20022, 2013.

Riddick, T., Brovkin, V., Hagemann, S., and Mikolajewicz, U.: Dynamic hydrological discharge modelling for coupled climate model simulations of the last glacial cycle: the MPI-DynamicHD model version 3.0, Geoscientific Model Development, 11, 4291–4316, https://doi.org/10.5194/gmd-11-4291-2018, 2018.

Ridley, J. K., Huybrechts, P., Gregory, J. M., and Lowe, J. A.: Elimination of the Greenland Ice Sheet in a High CO2 Climate, Journal of Climate, 18, 3409–3427, https://doi.org/10.1175/jcli3482.1, 2005.

Roberts, W. H., Valdes, P. J., and Payne, A. J.: A new constraint on the size of Heinrich Events from an iceberg/sediment model, Earth and Planetary Science Letters, 386, 1–9, https://doi.org/10.1016/j.epsl.2013.10.020, 2014.

Roche, D., Paillard, D., and Cortijo, E.: Constraints on the duration and freshwater release of Heinrich event 4 through isotope modelling, Nature, 432, 379–382, https://doi.org/10.1038/nature03059, 2004.

Roche, D. M., Dumas, C., Bügelmayer, M., Charbit, S., and Ritz, C.: Adding a dynamical cryosphere to amp;lt;iamp;gt;iamp;lt;/iamp;gt;LOVECLIM (version 1.0): coupling with the GRISLI ice-sheet model, Geoscientific Model Development, 7, 1377–1394, https://doi.org/10.5194/gmd-7-1377-2014, 2014.

Rovira-Navarro, M., van der Wal, W., Barletta, V. R., Root, B. C., and Sandberg Sørensen, L.: GRACE constraints on Earth rheology of the Barents Sea and Fennoscandia, Solid Earth, 11, 379–395, https://doi.org/10.5194/se-11-379-2020, 2020.

Schannwell, C., Mikolajewicz, U., Ziemen, F., and Kapsch, M.-L.: Sensitivity of Heinrich-type ice-sheet surge characteristics to boundary forcing perturbations, Climate of the Past, 19, 179–198, https://doi.org/10.5194/cp-19-179-2023, 2023.

Schannwell, C., Mikolajewicz, U., Kapsch, M.-L., and Ziemen, F.: A mechanism for reconciling the synchronisation of Heinrich events and Dansgaard-Oeschger cycles, Nature Communications, 15, https://doi.org/10.1038/s41467-024-47141-7, 2024.

Schiller, A., Mikolajewicz, U., and Voss, R.: The stability of the North Atlantic thermohaline circulation in a coupled ocean-atmosphere general circulation model., Climate Dynamics, p. 325–347, https://doi.org/https://doi.org/10.1007/s003820050169, 1997.

Schindlbeck-Belo, J. C., Toohey, M., Jegen, M., Kutterolf, S., and Rehfeld, K.: PalVol v1: a proxy-based semi-stochastic ensemble reconstruction of volcanic stratospheric sulfur injection for the last glacial cycle (140 000–50 BP), Earth System Science Data, 16, 1063–1081, https://doi.org/10.5194/essd-16-1063-2024, 2024.

Schmittner, A., Green, J. A. M., and Wilmes, S.: Glacial ocean overturning intensified by tidal mixing in a global circulation model, Geophysical Research Letters, 42, 4014–4022, https://doi.org/10.1002/2015gl063561, 2015.

Severinghaus, J. P. and Brook, E. J.: Abrupt Climate Change at the End of the Last Glacial Period Inferred from Trapped Air in Polar Ice, Science, 286, 930–934, https://doi.org/10.1126/science.286.5441.930, 1999.

Sherriff-Tadano, S., Ivanovic, R., Gregoire, L., Lang, C., Gandy, N., Gregory, J., Edwards, T. L., Pollard, O., and Smith, R. S.: Large-ensemble simulations of the North American and Greenland ice sheets at the Last Glacial Maximum with a coupled atmospheric general circulation–ice sheet model, Climate of the Past, 20, 1489–1512, https://doi.org/10.5194/cp-20-1489-2024, 2024.

Smith, R. S. and Gregory, J. M.: A study of the sensitivity of ocean overturning circulation and climate to freshwater input in different regions of the North Atlantic, Geophysical Research Letters, 36, https://doi.org/10.1029/2009GL038607, 2009.

Snoll, B., Ivanovic, R., Gregoire, L., Sherriff-Tadano, S., Menviel, L., Obase, T., Abe-Ouchi, A., Bouttes, N., He, C., He, F., Kapsch, M., Mikolajewicz, U., Muglia, J., and Valdes, P.: A multi-model assessment of the early last deglaciation (PMIP4 LDv1): a meltwater perspective, Climate of the Past, 20, 789–815, https://doi.org/10.5194/cp-20-789-2024, 2024.

Snyder, C. W.: Evolution of global temperature over the past two million years, Nature, 538, 226–228, https://doi.org/10.1038/nature19798, 2016.

Steffensen, J. P., Andersen, K. K., Bigler, M., Clausen, H. B., Dahl-Jensen, D., Fischer, H., Goto-Azuma, K., Hansson, M., Johnsen, S. J., Jouzel, J., Masson-Delmotte, V., Popp, T., Rasmussen, S. O., Röthlisberger, R., Ruth, U., Stauffer, B., Siggaard-Andersen, M.-L., Svein-björnsdóttir, A. E., Svensson, A., and White, J. W. C.: High-Resolution Greenland Ice Core Data Show Abrupt Climate Change Happens in Few Years, Science, 321, 680–684, https://doi.org/10.1126/science.1157707, 2008.

Stevens, B., Giorgetta, M., Esch, M., Mauritsen, T., Crueger, T., Rast, S., Salzmann, M., Schmidt, H., Bader, J., Block, K., Brokopf, R., Fast, I., Kinne, S., Kornblueh, L., Lohmann, U., Pincus, R., Reichler, T., and Roeckner, E.: Atmospheric component of the MPI-M Earth System Model: ECHAM6, Journal of Advances in Modeling Earth Systems, 5, 146–172, https://doi.org/10.1002/jame.20015, 2013.

Stouffer, R. J., Yin, J., Gregory, J. M., Dixon, K. W., Spelman, M. J., Hurlin, W., Weaver, A. J., Eby, M., Flato, G. M., Hasumi, H., Hu, A., Jungclaus, J. H., Kamenkovich, I. V., Levermann, A., Montoya, M., Murakami, S., Nawrath, S., Oka, A., Peltier, W. R., Robitaille, D. Y., Sokolov, A., Vettoretti, G., and Weber, S. L.: Investigating the causes of the response of the thermohaline circulation to Past and Future Climate Changes, Journal of Climate, 19, 1365 – 1387, https://doi.org/10.1175/JCLI3689.1, 2006.

Tarasov, L. and Peltier, W. R.: Arctic freshwater forcing of the Younger Dryas cold reversal, Nature, 435, 662–665, https://doi.org/10.1038/nature03617, 2005.

Tarasov, L., Dyke, A. S., Neal, R. M., and Peltier, W.: A data-calibrated distribution of deglacial chronologies for the North American ice complex from glaciological modeling, Earth and Planetary Science Letters, 315-316, 30 – 40, https://doi.org/https://doi.org/10.1016/j.epsl.2011.09.010, sea Level and Ice Sheet Evolution: A PALSEA Special Edition, 2012.

Tierney, J. E., Zhu, J., King, J., Malevich, S. B., Hakim, G. J., and Poulsen, C. J.: Glacial cooling and climate sensitivity revisited, Nature, 584, 569–573, https://doi.org/10.1038/s41586-020-2617-x, 2020.

Vizcaíno, M., Mikolajewicz, U., Gröger, M., Maier-Reimer, E., Schurgers, G., and Winguth, A. M. E.: Long-term ice sheet–climate interactions under anthropogenic greenhouse forcing simulated with a complex Earth System Model, Climate Dynamics, 31, 665–690, https://doi.org/10.1007/s00382-008-0369-7, 2008.

Vizcaíno, M., Mikolajewicz, U., Ziemen, F., Rodehacke, C. B., Greve, R., and van den Broeke, M. R.: Coupled simulations of Greenland Ice Sheet and climate change up to A.D. 2300, Geophysical Research Letters, 42, 3927–3935, https://doi.org/https://doi.org/10.1002/2014GL061142, 2015.

Weaver, A. J., Saenko, O. A., Clark, P. U., and Mitrovica, J. X.: Meltwater Pulse 1A from Antarctica as a Trigger of the Bølling-Allerød Warm Interval, Science, 299, 1709–1713, https://doi.org/10.1126/science.1081002, 2003.

Wilmes, S., Schmittner, A., and Green, J. A. M.: Glacial Ice Sheet Extent Effects on Modeled Tidal Mixing and the Global Overturning Circulation, Paleoceanography and Paleoclimatology, 34, 1437–1454, https://doi.org/10.1029/2019pa003644, 2019.

Wunsch, C.: Determining paleoceanographic circulations, with emphasis on the Last Glacial Maximum, Quaternary Science Reviews, 22, 371–385, https://doi.org/10.1016/s0277-3791(02)00177-4, 2003.

Zhao, N., Oppo, D. W., Huang, K.-F., Howe, J. N. W., Blusztajn, J., and Keigwin, L. D.: Glacial–interglacial Nd isotope variability of North Atlantic Deep Water modulated by North American ice sheet, Nature Communications, 10, https://doi.org/10.1038/s41467-019-13707-z, 2019.

Ziemen, F. A., Rodehacke, C. B., and Mikolajewicz, U.: Coupled ice sheet–climate modeling under glacial and pre-industrial boundary conditions, Climate of the Past, 10, 1817–1836, https://doi.org/10.5194/cp-10-1817-2014, 2014.

Ziemen, F. A., Kapsch, M.-L., Klockmann, M., and Mikolajewicz, U.: Heinrich events show two-stage climate response in transient glacial simulations, Climate of the Past, 15, 153–168, https://doi.org/10.5194/cp-15-153-2019, 2019.

Ziemen, F. A., Mikolajewicz, U., Kapsch, M.-L., Schannwell, C., Six, K. D., Bagge, M., Baudouin, J.-P., Erokhina, O., Gayler, V., Klemann, V., Meccia, V. L., Mouchet, A., and Riddick, T.: Coupled climate-ice sheet simulation of the last deglaciation, Copernicus Publications, https://doi.org/10.5446/69659, https://doi.org/10.5446/69659, 2024.

Table A1. Individual parameter settings for each model component across the ensemble members and corresponding spin-up simulation. In all asynchronous spin-up simulations climatological volcanic forcing was used.

Name	MPI-ESM	Volcanoes	PISM_ANT	PISM_NH	Asynchronous spin-up
D1.1	version 1	fixed	version 1	version 1	- parameters as in synchronous simulation
D1.2	version 1 dback 1.5×10^{-5}	fixed	version 1	version 1	- parameters as in synchronous simulation D1.1
D1.3	version 1 dback 0.7×10^{-5}	fixed	version 1	version 1	- parameters as in synchronous simulation D1.1
D1.4	version 1	varying	version 1	version 1	- parameters as in synchronous simulation D1.1
D2.1	version 2 ECHAM: crs 0.985 crt 0.87 cvtfall 2.8 MPIOM: hiccp 27 cw 0.001 dbackprofile 5 dback 4.2×10^{-6}	varying	version 2 sliding_scale_factor_reduces_tauc 1.8 th_heat_coefficient 10^{-2}	version 2 sliding_scale_factor_reduces_tauc 1.8 th_heat_coefficient 10^{-2} topg_to_phi 8.5, 23.5, -300.0, 400.0	- parameters as in synchronous simulation
D2.2	version 2 atmosphere as in version 1	varying	version 2	version 2	- parameters as in synchronous simulation
D2.3	version 2 surface mass balance module: alb_frsnow 0.92 alb_icerefrz 0.55 alb_icemelt 0.55	varying	version 2	version 2	- parameters as in synchronous simulation
D2.4	version 2	varying	version 1 topg_to_phi 14.0, 30.0, -300.0, 400.0	version 2	- parameters as in synchronous simulation
D2.1.1[a,b]	version 2	varying	version 2	version 2	- parameters as in synchronous simulation D2.1 - ice sheets and solid earth from 27 ka
D2.1.2[a]	version 2	varying	version 2	version 2	- parameters as in synchronous simulation D2.1 - ice sheets and solid earth from 28 ka

[a] The sensitivity studies D2.1.1 and D2.1.2 are not part of the ensemble, [b] D.2.1.1 was run only until 7 ka

Table A2. List of all parameters and their full name as well as standard value that were varied across the ensemble members.

Parameter	Explanation	Standard Value
ECHAM		
crs	relative humidity threshold for cloud formation in the lowest model level	0.98
crt	relative humidity threshold for cloud formation in the upper troposphere	0.85
cvtfall	fall speed of cloud ice	2.9
MPIOM		
hiccp	ice strenth parameter P* in the Hibler model	20
cw	drag coefficient between sea ice and water	0.0045
dbackprofile	ratio between the value near the surface and below 1000 m of the background diffusivity in the ocean	3
dback	surface background diffusivity	1.05×10^{-5}
EBM		
alb_frsnow	albedo of fresh snow	0.91
alb_icerefrz	albedo of refrozen ice	0.545
alb_icemelt	melt albedo of ice	0.54
mPISM		
sliding_scale_factor_reduces_tauc	constant that divides pseudo-plastic tauc (yield stress) by given factor	1
topg_to_phi	piece-wise linear function of till friction angle	15, 30, -300, 400.0
th_heat_coefficient	coefficient for turbulent heat exchange from ambient ocean to ice shelf	4×10^{-5}

Table A3. Ice volumes in $\times 10^{15}$ m^3 of major ice sheets for all simulations at the LGM and PI

Name	Laurentide	Fennoscandian	Greenland	Antarctica
LGM				
D1.1	23.53	8.33	3.84	31.56
D1.2	23.27	8.24	3.85	31.37
D1.3	24.44	8.47	3.82	31.52
D1.4	23.71	8.40	3.83	31.50
D2.1	22.83	8.16	3.78	28.92
D2.2	21.17	4.45	3.51	28.95
D2.3	21.88	6.73	3.53	29.27
D2.4	21.17	4.61	3.50	30.71
GLAC-1D	26.51	6.16	4.03	31.17
ICE-6G	30.12	6.38	4.14	31.90
PI				
D1.1	1.09	0.06	3.48	34.07
D1.2	0.94	0.04	3.41	32.46
D1.3	1.41	0.21	3.50	34.05
D1.4	1.16	0.06	3.48	34.05
D2.1	1.41	0.23	3.38	27.71
D2.2	1.05	0.03	3.31	27.22
D2.3	1.35	0.04	3.36	27.18
D2.4	0.71	0.03	3.25	30.55
GLAC-1D	0.18	0.01	3.07	26.18
ICE-6G	0.04	0.00	3.05	26.35